ABSTRACT

Title of Thesis:	**Characterizing 3-dimensional Melt Distribution and Anisotropic Permeability in Sheared Partially Molten Rocks**
	James Alexander Bader, Master of Science, 2020
Thesis Directed By:	Dr. Wenlu Zhu (Professor) Dr. Laurent Montesi (Professor) Department of Geology

With increasing shear strain, initially homogeneously distributed melt can segregate into an array of melt-rich bands, flanked by melt-poor regions. To address how the formation of these melt-rich bands affects the transport properties of partially molten rocks, I analyzed X-ray synchrotron microtomographic images of an aggregate composed of 10 vol% basaltic melt and 90 vol% olivine that was sheared to a total strain of 13.3. At 0.16 μm per pixel, the spatial resolution of the microtomographic dataset is sufficiently high for quantitative characterization of 3-dimensional melt distribution. The results show that the melt distribution is bimodal: in the melt-poor regions, the total melt fractions range from 0.078-0.100, with no interconnected melt; in the melt-rich regions, the total melt fractions range from 0.116 to 0.178, with the interconnected melt fraction ranging from 0.08 to 0.16. The permeability of the sample was calculated using a digital rock physics approach. Along a melt-rich band, permeability (k) as function of melt fraction (ϕ) and grain size (d) can be expressed as $k = \frac{\phi^{3.2} d^2}{12.4}$. Between melt-rich bands, the permeability is

negligible. Thus, the permeability of the sheared partially molten rock is highly anisotropic and negligible in the direction perpendicular to the bands. Grain size measurements were obtained through electron backscatter diffraction. After adjusting for grain size, the permeability of a sheared partially molten rock measured along the direction of melt bands is higher than that of its isotropic counterpart with the same bulk melt fraction. The strong anisotropic permeability provides new insight into the effect of melt band formation on melt migration and melt focusing at mid ocean ridges.

Characterizing 3-dimensional Melt Distribution and Anisotropic Permeability in Sheared Partially Molten Rocks

by

James Alexander Bader

Thesis submitted to the Faculty of the Graduate School of the
University of Maryland, College Park, in partial fulfillment
of the requirements for the degree of
Master of Science
2020

Advisory Committee:

Professor Wenlu Zhu, Chair (University of Maryland)
Professor Laurent Montesi (University of Maryland)
Assistant Professor Megan Newcombe (University of Maryland)

Table of Contents

List of Tables

List of Figures

Figure 5: Sample CQ0705 (~2 mm long and ~0.9mm in diameter) was cored from a sheared partially molten rock PT0705 (10 mm long, 5 mm in diameter). The red dash lines represent melt-rich bands.

Figure 6: A conceptual diagram showing the workflow of X-ray synchrotron microtomography and digital rock physics. The absorption of X-ray beam passing through different phases in a rock sample is mapped and the radiograph is collected by a CCD camera after a scintillator turned the X-ray energy into visible light. Successive 2D radiographs can be collected as the sample rotates, enabling the 3D reconstruction of the rock. The microtomographic data is then processed to obtain the 3D melt distribution can be obtained. The permeability can be calculated using flow simulations through the digital rock constructed using the 3D melt distribution.

Figure 7: A 2D slice within a 3D micro-tomography dataset of sample CQ0705. The darker gray represent the basaltic melt, while the lighter gray represents the olivine grains. A melt-rich band is outlined in red. The black box represents a subvolume which will be filtered and segmented in Figures 8-10. Solid olivine, basaltic melt and scale bars are marked.

Figure 8: The region within the black box in this image has been smoothed using an anisotropic diffusion filter, the one chosen to be most effective. While the amount of random noise present before smoothing has been greatly reduced, the portions that correspond to the basaltic melt are well preserved.

Figure 9: 2-D slice of the three-dimensional thresholded region, where the black represents solid (olivine), and the blue color denotes the pore space (occupied by

basalt). This was produced by the *interactive thresholding* module, where the range of grayscale values that were visually observed as melt was selected.

Figure 10: A final filter, *remove small spots*, was used to remove the final spots below 10 pixels in size. At this pixel size, the connectivity results were not affected, tested by measuring the connectivity sample-wide with and without using this module.

Figure 11: Rotation of sample CQ0705. After a rotation of 344º around the S_X axis, and 20º around the S_Z axis, the X and Z axes are along melt bands, and the Y axis is across melt bands.

Figure 12: Different subvolume configurations selected from the fully thresholded sample CQ0705. The subvolume in red is 128x24x24 μm^3. The green region represents subvolumes where the fluid inflow and outflow region is kept the size of the red subvolume, but the flow can meander outside this restricted region so long as it stays within the green extended subvolume. The yellow subvolume corresponds to the large subvolume discussed in the connectivity and permeability section, is 128x128x128 μm^3 in size and contains both melt poor and melt rich regions.

Figure 13: Conceptual diagram of the *absolute permeability experimental solution* (APES) in Avizo. Flow is initiated in the X direction by pressure gradient, with no flow in other directions by way of an impermeable boundary layer added to four of the six subvolume faces. The region is padded at the start and end to ensure there is no bias towards the large pore space in initial flow through the subvolume face.

Figure 14: Calculation showing the APES using the extended domain subvolumes for permeability calculation. The inlet is kept the same while the domain is extended. This

allows fluid flow paths that go outside the subvolume to be included in the flow field, so long as the fluid returns to the region between the inlet and outlet of the subvolume.

Figure 15: Histogram of melt fractions of 23 subvolumes. The size of each subvolumes is 128x24x24 μm^3. Which is taken either entirely within a melt band, or completely outside melt bands. Within melt bands, melt fraction ranges from 0.109 to 0.178. Outside melt bands, melt fraction ranges from 0.078 to 0.098.

Figure 16: Subvolume 128x128x128 μm in size, with connected pore space in the X direction shown in red, and disconnected pore space shown in gray. The connected regions in red are the planar melt-rich bands, and the gray regions in between are the melt poor region where there is little to no connectivity found.

Figure 17: Subvolume taken within a melt band, 128x24x24 μm in size. The connected pore-space is shown in red, and the disconnected pore space in gray.

Figure 18: Subvolume taken outside of a melt band, 128x24x24 μm in size. All pore space is disconnected, shown in gray. This pore space is disconnected in the X, Y, and Z direction.

Figure 19: Graph showing melt fraction versus connected melt fraction for subvolumes taken throughout sample CQ0705. The gray-filled squares correspond to connected melt fraction for subvolumes 128 μm long in the Z direction, while the empty symbols correspond to connected melt fraction for subvolumes 128 μm long in the X direction. The black square represents a subvolume 128 μm long in each direction, which contains both melt poor and melt-rich regions (gray subvolume Figure 11). A trend line is shown for the subvolumes that have some connected melt, and are 128x24x24 μm^3 in dimension. They represent subvolumes inside the melt band.

Figure 20: Image of two flowpath animations, produced by the APES velocity field in Avizo. The yellow flowlines denote fluid flow at a point in time through the 128x24x24 subvolume, while the right subvolume is the same region with an extended domain permitted for fluid flow. The axis are notated, with the long axis of calculation in the X direction.

Figure 21: Permeability versus melt fraction in a log-log plot. Data was collected using the LBM. All data shown was collected in the X direction within sample CQ0705. The blue line shows trend fitted to the regular subvolumes (circle symbols), while the red is for the extended domain calculations (diamond symbols).

Figure 22: Permeability versus melt fraction in a log-log plot. These data show permeability results for the other along-band direction, the Z direction, where extended domain subvolume data is shown with red diamonds filled in gray, fitted by a dashed red line, and 24x24x128 μm^3 subvolume data denoted by blue circles fit by a dashed blue line.

Figure 23: Summary log-log plot including all permeability versus porosity calculations for CQ0705 using the LBM, in both along-band directions.

Figure A1: An overview of EBSD methodology. Polished rock sample is loaded and pelted with electrons, where the excited electron cloud is picked up by a detector, and diffraction patterns are reconstructed by collection software. Pixel orientations of a mapped area can then be exported and processed.

Figure A2: Top left: EBSD data. Top right: Grain reconstruction of the region boxed in red from the EBSD data. Bottom: Histogram of grain size. The mean grain size of 2.28 □m from the best fit of the histogram is reported in Table 2.

Figure A3: Top left: EBSD data. Top right: Grain reconstruction of the region boxed in red from the EBSD data. Bottom: Histogram of grain size. The mean grain size of 2.29 □m from the best fit of the histogram is reported in Table 2.

Figure A4: Top left: EBSD data. Top right: Grain reconstruction of the region boxed in red from the EBSD data. Bottom: Histogram of grain size. The mean grain size of 2.48 □m from the best fit of the histogram is reported in Table 2.

Figure A5: Top left: EBSD data. Top right: Grain reconstruction of the region boxed in red from the EBSD data. Bottom: Histogram of grain size. The mean grain size of 2.72 μm from the best fit of the histogram is reported in Table 2.

Figure A6: Top left: EBSD data. Top right: Grain reconstruction of the region boxed in red from the EBSD data. Bottom: Histogram of grain size. The mean grain size of 2.15 μm from the best fit of the histogram is reported in Table 2.

Figure A7: Top left: EBSD data. Top right: Grain reconstruction of the region boxed in red from the EBSD data. Bottom: Histogram of grain size. The mean grain size of 2.15 μm from the best fit of the histogram is reported in Table 2.

Figure A8: Top left: EBSD data. Top right: Grain reconstruction of the region boxed in red from the EBSD data. Bottom: Histogram of grain size. The mean grain size of 2.28 μm from the best fit of the histogram is reported in Table 2.

Figure A9: Top left: EBSD data. Top right: Grain reconstruction of the region boxed in red from the EBSD data. Bottom: Histogram of grain size. The mean grain size of 2.58 μm from the best fit of the histogram is reported in Table 2.

Figure A10: Top left: EBSD data. Top right: Grain reconstruction of the region boxed in red from the EBSD data. Bottom: Histogram of grain size. The mean grain size of 2.43 μm from the best fit of the histogram is reported in Table 2.

Figure A11: Top left: EBSD data. Top right: Grain reconstruction of the region boxed in red from the EBSD data. Bottom: Histogram of grain size. The mean grain size of 2.48 μm from the best fit of the histogram is reported in Table 2.

Figure A12: Top left: EBSD data. Top right: Grain reconstruction of the region boxed in red from the EBSD data. Bottom: Histogram of grain size. The mean grain size of 2.62 μm from the best fit of the histogram is reported in Table 2.

Figure A13: Top left: EBSD data. Top right: Grain reconstruction of the region boxed in red from the EBSD data. Bottom: Histogram of grain size. The mean grain size of 2.90 μm from the best fit of the histogram is reported in Table 2.

Figure A14: Top left: EBSD data. Top right: Grain reconstruction of the region boxed in red from the EBSD data. Bottom: Histogram of grain size. The mean grain size of 2.75 μm from the best fit of the histogram is reported in Table 2.

Figure A15: Top left: EBSD data. Top right: Grain reconstruction of the region boxed in red from the EBSD data. Bottom: Histogram of grain size. The mean grain size of 2.76 μm from the best fit of the histogram is reported in Table 2.

Figure A16: Top left: EBSD data. Top right: Grain reconstruction of the region boxed in red from the EBSD data. Bottom: Histogram of grain size. The mean grain size of 2.93 μm from the best fit of the histogram is reported in Table 2.

Figure A17: Top left: EBSD data. Top right: Grain reconstruction of the region boxed in red from the EBSD data. Bottom: Histogram of grain size. The mean grain size of 3.08 μm from the best fit of the histogram is reported in Table 2.

Chapter 1: Introduction

1.1: Motivation

Mid ocean ridges (MORs), one of the primary structures associated with plate tectonics, are the most volcanically active features on Earth. The new crust produced at these boundaries offer a glimpse into mantle dynamics and Earth composition, where upwelling magma travels roughly one hundred kilometers through the upper mantle to produce juvenile crust. Since the discovery of seafloor spreading and the acceptance of plate tectonics, great efforts have been made to understand these divergent boundaries, using various geochemical, geophysical, and geodynamical methods. With rapid melt extraction, Ahern and Turcotte (1979) predicted that only 2-3% melt would be retained in the mantle, which is corroborated by seismic evidence. Direct measurements of melt migration beneath mid ocean ridges is especially challenging since the depths where melting occurs are kilometers beneath the Earth's surface, while the deepest samples come from perhaps a kilometer below the ocean floor (Frey et al., 1974). Seismic tomography is useful for broad observations at greater depths, yet still lacks resolution for small-scale features in the upper mantle. For instance, shallow imaging targeting tens of kilometers beneath the surface has a resolution of kilometers (Dunn et al., 2017). Features at greater depths have even lower resolution.

Holtzman et al. (2003) showed at shear strain (γ) of 2 or greater, partial melt segregates into discrete melt rich regions. These planar regions were named melt-rich bands (or simply melt bands). The formation of these melt-rich bands can result in anisotropic permeability and viscosity (e.g., Katz et al., 2006; Kohlstedt and Holtzman,

2009) and thus affects melt transport in these regions. While Zimmerman et al. (1999) discusses potential permeability anisotropy due to melt pocket alignment, the permeability of sheared partially molten rocks has yet to be quantified.

X-ray synchrotron microtomography is shown to be effective for studying the 3D melt distribution in partially molten mantle rocks (Zhu et al., 2011). Based on the high resolution 3D microtomographic images, digital rocks can be constructed. Physical properties such as permeability and electrical conductivity can then be calculated by conducted flow simulations on the digital rock (Miller et al., 2014; 2016). Using X-ray synchrotron microtomography and digital rock physics methods, this study focuses on quantifying melt connectivity and permeability in a partially molten rock that has undergone shear deformation.

1.2: Mid Ocean Ridge Overview

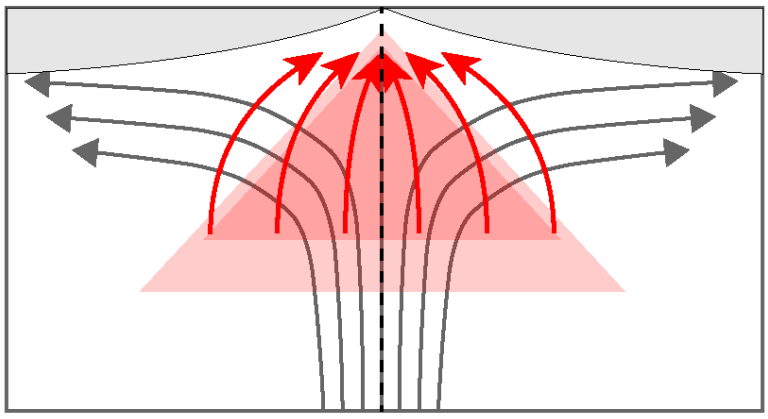

Figure 1: Mid ocean ridge (MOR) cross-section. The black dashed line represents the spreading axis. Gray lines with arrowheads show the divergent upwelling mantle beneath MOR. High shear strain is expected near the spreading axis where the flow direction changes. The red triangles represent partially molten regions beneath MOR, with the primary melting region shown in light red and increased melt

concentration shown in dark red (MELT seismic team, 1998). Red lines with arrowheads represent melt migration and focusing beneath MOR.

Beneath MORs, melt extract is expected to be very efficient. Of the 20% partial melting. Ahern & Turcotte (1979) suggested that only 2-3% of melt would be retained at any time. Using seismic and magnetotelluric data, the MELT Seismic team (1998) found that beneath the East Pacific Rise (EPR) at 17°S, there is roughly 1-3% melt. However, a more recent study using magnetotelluric methods found that there are ~10% melt at EPR 9'30º N (Key et al., 2013).

In contrast, geochemical data on uranium decay series isotopes indicate extremely rapid melt segregation. To preserve the short-lived radium and thorium isotopes observed in mid ocean ridge basalts (e.g., Johnson et al., 1990; Lundstrom et al., 1995, 1998, 1999, 2000; Salters and Longhi, 1999), melt fractions must be below 1% for a well-connected permeable upper mantle.

To reconcile geochemical evidence and the geophysical observations, it has been proposed melt must segregate into channels of high permeability that are responsible for most of the melt transport beneath mid ocean ridges (Spiegelman & Kenyon, 1992). Example of channelized flow are observed in ophiolites (Braun and Kelemen, 2002). It has been shown that reaction infiltration instability (e.g., Kelemen et al., 1997) as well as large shear strain (e.g., Zimmerman et al., 1999; Holtzman et al., 2003) can induce melt channelization in partially molten rocks.

1.3: Partial Melt Response to Deformation

Zimmerman et al. (1999) demonstrated experimental partially molten aggregates subjected to simple shear will develop a heterogeneous melt distribution, where melt becomes channelized. Further experimental evidence of shear-induced melt channelization was shown by Holtzman et al. (2003), with planar melt-rich bands shown to develop at absolute strain of ~2 or greater, with corresponding melt poor regions in between. Holtzman et al. (2003) proposed the melt bands would form in partially molten regions at subduction wedges, mantle plumes, and mid-ocean ridges, where high shear strain occurs.

For a texturally equilibrated partially molten rock with homogenous melt distribution, a power-law relationship between the permeability and melt fraction can be deduced (e.g., von Bargen and Waff, 1986). The formation of melt bands could have a direct impact on permeability. Zimmerman et al. (1999) found that olivine-basalt aggregates subjected to strains ~2 or greater develop a melt-pocket orientation (MPO), as melt pockets oriented ~20 degrees from the shear plane experience lower differential stress near the pocket tips and preferentially grow compared to other orientations. They argue that if permeability is proportional to melt pocket area, permeability ought to be anisotropic where permeability (k) in the direction of MPO would be ~5 times greater than across this direction. Holtzman et al. (2003) attempted to further calculate the permeability anisotropy from 2-dimensional (2D) images, and estimated that permeability across the melt bands could be an order of magnitude lower than the permeability along the melt bands. Due to the lack of quantitative constraints on melt connectivity, the estimated permeability in these studies remain highly uncertain.

More recent experimental studies utilized a torsion apparatus to shear the partially molten samples to much larger strains (King et al., 2010; Qi et al., 2015, 2018). Qi et al. (2015, 2018) observed melt bands and MPO development as a result of shear similar to previous studies, in addition to the rotation of olivine axis in a partially molten system undergoing shear compared to a melt-free aggregate undergoing shear, which could have implications for seismic anisotropy. One of the olivine-basalt aggregates was sheared to a total strain of 13.3 at 1200°C and 300MPa using a torsion apparatus Qi et al. (2014). The sample used in this study was taken from this experimental charge.

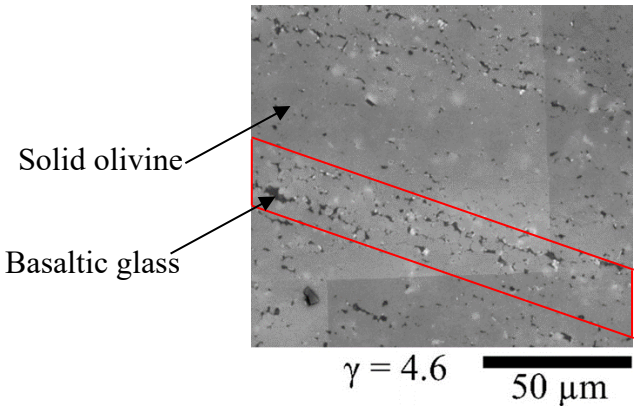

Figure 2: An SEM image of a sheared (strain = 4.6) partially molten olivine-basalt aggregate. Melt pockets (basaltic glass) are darker gray, olivine grains are light gray, and internal reflections or residual polishing material are white (Qi et al., 2015). A melt band is boxed in red. The solid olivine grain, the basaltic glass and the scale bar are marked.

Substantial work has been done to quantify the development of MPO, melt band orientation, 2D melt distribution, and olivine grain orientation in sheared partially molten rocks. To date, the 3D melt distribution and permeability of these rocks remain poorly constrained. Quantifying transport properties of sheared partially molten rocks

is crucial to understand melt migration beneath mid ocean ridges, where shear strain is expected to occur due to mantle upwelling as discussed by Katz et al. (2006).

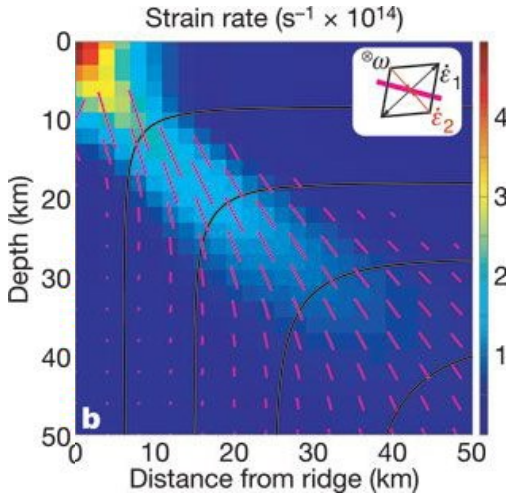

Figure 3: Solution for a numerical model of a mid-ocean ridge, where the ridge is in the top left corner of the plot. The black lines represent mantle flow lines, while the color shows strain rate. The magenta lines are expected melt band orientations, with the length of these representative of the local strain rate. Figure taken from Katz et al. (2006).

It has been proposed that the melt bands that develop from shear could orient towards the mid-ocean ridge axis by numerical modeling work that, when accounting for non-newtonian viscosity in melt band formation, best match experimental melt band orientation (Katz et al., 2006). This work suggests that, given a melt band angle of 25º from the shear plane as found in experiments in Holtzman et al. (2003), and if permeability is higher along the melt bands, shear strain could promote rapid melt extraction towards the mid-ocean ridge axis, with little permeability across the melt bands. While melt band orientation beneath mid ocean ridges is not certain (e.g., Butler 2009), it is necessary to quantify permeability of a partially molten system under shear,

specifically the potential anisotropy, when comparing along band versus across band permeability.

1.4: X-ray Synchrotron Microtomography and Digital Rock Physics

Melt flow velocity is dependent on the permeability of the partially molten rock (McKenzie 1984). For a texturally equilibrated partial molten rocks, theoretical and numerical studies show that permeability (k) as function of melt fraction (ϕ) and grain size (d) can be expressed as a power-law (equation 1) where C is a geometric constant and the exponent n is either 2 or 3 (e.g., von Bargen and Waff, 1986, Zhu and Hirth, 2003).

$$k = \frac{\phi^n d^2}{C} \quad (1)$$

Using X-ray synchrotron microtomography and digital rock physics methods, Zhu et al. (2011) and Miller et al. (2014, 2015, 2016) quantified the 3D melt distribution and permeability of partially molten aggregates. They showed a power-law relationship between permeability and total melt fraction with an power-law exponent of 2.6 (Figure 4), with a geometric factor C of 58:

$$k = \frac{\phi^{2.6} d^2}{58} \quad (2)$$

The permeability-melt fraction relationship of partially molten rocks obtained by Miller et al. (2015) is in a good agreement with previous theoretical and numerical results (e.g., Smith 1964; von Bargen and Waff, 1986; Zhu and Hirth, 2003).

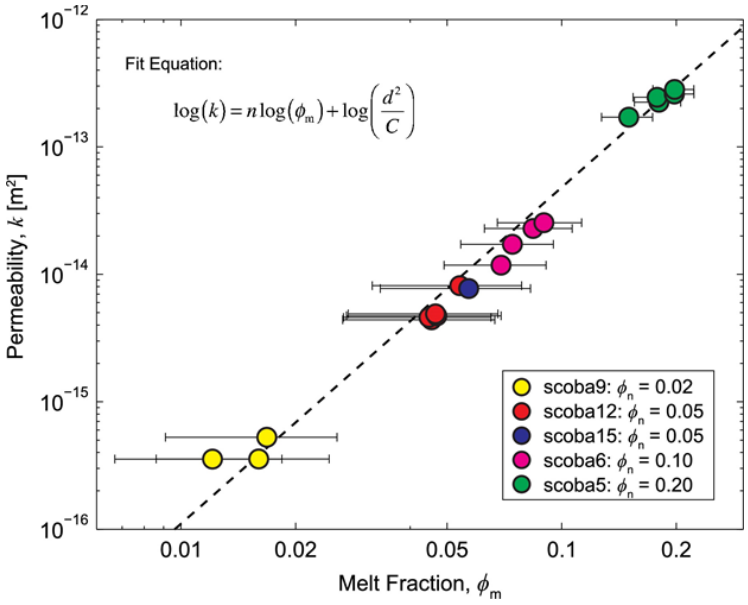

Figure 4: Permeability (k) is plotted against melt fraction (ϕm) of each subvolume from 5 different partially molten olivine-basalt aggregates. The initial melt volume fraction (ϕn) for each aggregate is given in the legend. Data is fit by a power law relationship (the top left), with an exponent 'n' of 2.6. Taken from Miller et al., 2014.

1.5: Aim of this Study

To date, the 3D melt distribution and permeability of sheared partially molten rocks are still unknown. Quantitative characterization of how the shear-induced melt bands affect transport properties of partially molten rocks is critical for better understanding of melt migration and focusing at MORs (e.g., Katz et al., 2006).

In this study, X-ray synchrotron microtomography and digital rock physics were used to quantify the 3D melt distribution and permeability of an olivine-basalt aggregate sheared to a total strain of 13.3. Avizo and PerGeos © ThermoFisher Scientific were used to filter the 3D microtomographic images, measure melt fraction throughout the sample, and perform digital flow simulations to calculate permeability. To measure the grain size, electron backscatter diffraction imagery was collected and

processed using Chanel5, Aztec © Oxford Instruments software as outlined in Qi et al. (2015, 2018), then MTEX (Bachmann et al., 2010). The obtained grain size was used to normalize permeability values of different systems for comparisons. This study aims at getting the first quantitative constraint on 3D melt distribution and permeability of partially molten rocks that consist of shear-induced melt bands, with quantifying shear-induced melt channels. The results show significant permeability anisotropy, heterogeneous melt distribution, and provide an effective mechanism for melt focusing towards mid ocean ridges.

Chapter 2: Methods

2.1: Sample Background

A cylindrical core CQ0705 of ~2mm long and ~0.9 mm in diameter was taken from a sheared partially molten olivine-basalt aggregate PT0705 (Qi et al., 2015, 2018). The aggregate PT0705 consists of a homogeneous mixture of 90% San Carlos olivine and 10% MORB, ground to a particle size <3 μm. The sample was heated to 1473K at 300MPa confining pressure for approximately two hours, to ensure the sample was anhydrous and free of carbon impurities. The sample was then deformed using a torsion apparatus for several hours to a maximum strain of 13.3. Once this strain was achieved, the sample was quenched to preserve the melt microstructure at the time of deformation. A drillcore (sample CQ0705) was taken from the surface of PT0705 (Figure 5).

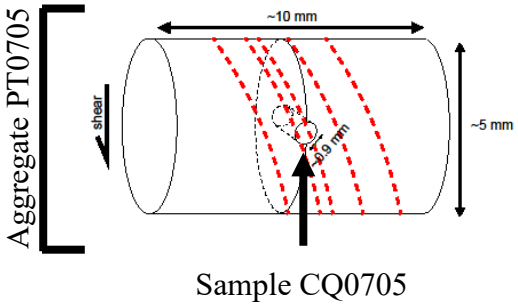

Figure 5: Sample CQ0705 (~2 mm long and ~0.9mm in diameter) was cored from a sheared partially molten rock PT0705 (10 mm long, 5 mm in diameter). The red dash lines represent melt-rich bands.

2.2: 3D Image Processing

Previous studies used X-ray synchrotron microtomography to obtain the 3D melt distribution (Zhu et al., 2011) of textually equilibrated partially molten rocks and quantified transport properties using digital rock physics models (Miller et al., 2014, 2015, 2016). - Similar approaches are adopted in this study to quantify melt fraction, melt connectivity, and permeability of the sheared partially molten rock.

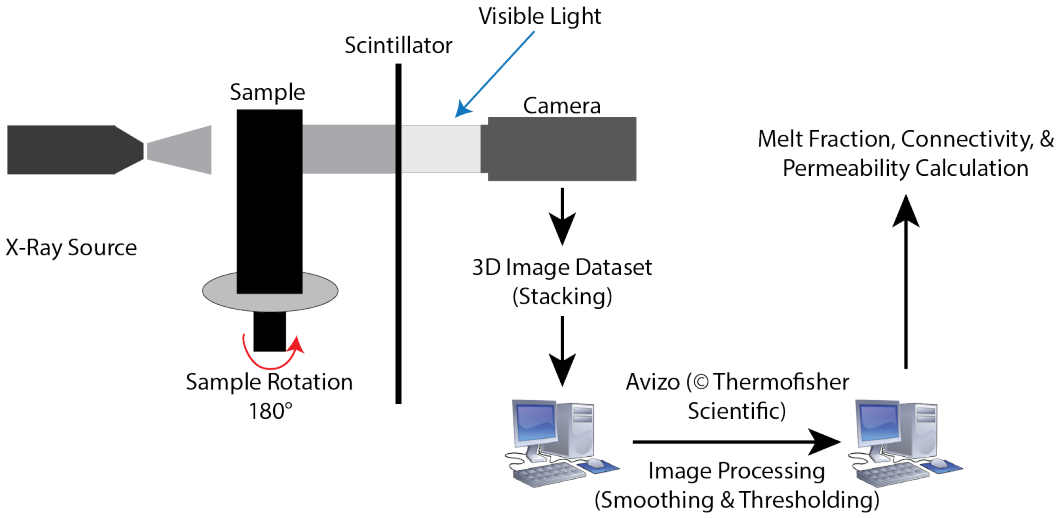

Figure 6: A conceptual diagram showing the workflow of X-ray synchrotron microtomography and digital rock physics. The absorption of X-ray beam passing through different phases in a rock sample is mapped and the radiograph is collected by a CCD camera after a scintillator turned the X-ray energy into visible light. Successive 2D radiographs can be collected as the sample rotates, enabling the 3D reconstruction of the rock. The microtomographic data is then processed to obtain the 3D melt distribution can be obtained. The permeability can be calculated using flow simulations through the digital rock constructed using the 3D melt distribution.

As X-ray beam passing through the rock sample, absorption by different phases varies. X-ray imaging is generated based on the absorption map. Because the contrast between basalt and olivine (3000 kg/m^3 and 3300 kg/m^3, respectively) is small, a phase-

contrast imaging technique is used to obtain the 3D melt distribution in partially molten rocks (Zhu et al., 2011). In this study, 3D images of CQ0705 were collected using phase constrast X-ray synchrotron microtomography at the European Synchrotron Radiation Facility (ESRF). The spatial resolution is 0.16 μm per pixel. At this resolution, the 3D melt geometry can be quantified (Figure 7).

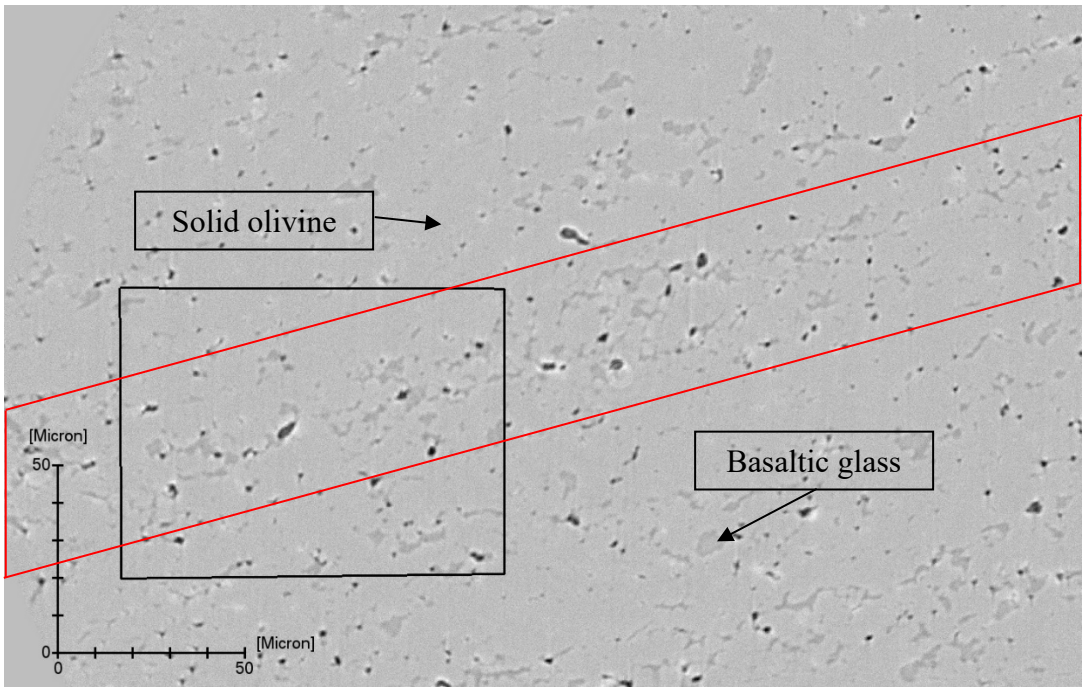

Figure 7: A 2D slice within a 3D micro-tomography dataset of sample CQ0705. The darker gray represent the basaltic melt, while the lighter gray represents the olivine grains. A melt-rich band is outlined in red. The black box represents a subvolume which will be filtered and segmented in Figures 8-10. Solid olivine, basaltic melt and scale bars are marked.

To obtain the 3D melt distribution, one must segment the melt from the solid. It can be seen that in a tomographic image (Figure 7), the range of grayscale values for melt are different from those of olivine. Segmentation of melt from olivine is based on the difference in grayscale values. However, it is common that there are very localized

fluctuations in grayscale values within the solid or melt. These fluctuations are noises in the microtomographic images that must be removed for better segmentation results. Various filters are used to reduce noises, and the segmentation is done on filtered images. Because there are only two phases in CQ0705, after segmentation, the two phases are assigned either a 1 or 0 value. This assignment, or thresholding, is done so that further analyses can be made on the digital space representing the melt versus solid.

All 3D image processing (and further quantification of melt topology and permeability) are done in Avizo (© ThermoFisher Scientific) version 9.4, Avizo XLab Hydro and PerGeos 2019. A series of filters were tested, including an edge-preserving smoothing filter, an anisotropic diffusion filter, a gaussian filter, as well as watershed-thresholding methods. It was decided that the filter that best preserved the melt microstructure while reducing noise to the minimal level was the anisotropic diffusion filter (Miller et al., 2015). The findings here are supported by literature (e.g., Weickert 1999), which found when comparing many of the same filters, that anisotropic diffusion filtering methods are shown to reduce noise effectively from X-ray image datasets. Several observations were consistent between Weickert (1999) and the filtering of this dataset, including the inaccurate whitening and expanding of edges near a sharp contrast (such as an olivine-basalt contact) when using the gaussian filter, and less effective image reduction when using an edge-preserving smoothing filter when compared to the anisotropic diffusion filter. Each filtered and thresholded image was compared against the original, in both 2D and 3D, to ensure melt microstructure was adequately preserved and the noise reduction was optimal.

The anisotropic diffusion filter works by comparing neighboring pixels to the six that touch it, and determining whether to keep the assigned value or adjust it based on the difference between the pixels and a local average. By increasing the threshold and iteration step, smoothing increases until eventually all pixels will have the same value. By keeping the iterations and diffusion threshold low, change is minimal, and the image is close to the original. Various settings were tested within each filter, until the final image had minimal noise that could interfere with image thresholding while preserving the contrast between the olivine and basalt (Figure 8).

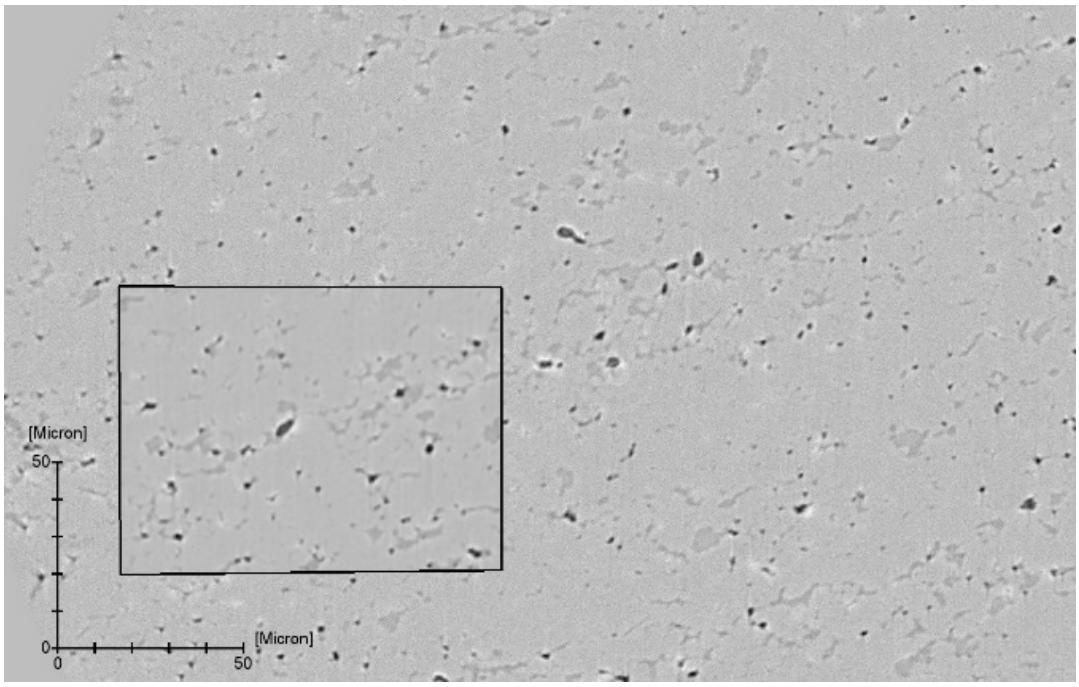

Figure 8: The region within the black box in this image has been smoothed using an anisotropic diffusion filter, the one chosen to be most effective. While the amount of random noise present before smoothing has been greatly reduced, the portions that correspond to the basaltic melt are well preserved.

Following image smoothing, the images were thresholded to create a binary digital rock which represents the deformed rock. A series of methods were again tested,

with interactive thresholding determined to be most effective. A value of 48100 selected for the grayscale cutoff between melt and solid (Figure 9). A final step to remove remnants of the noise that was not eliminated by the anisotropic diffusion filter, was to remove all spots smaller than 10 pixels using the *remove small spots* module in Avizo (Figure 10). This final step is necessary because the anisotropic diffusion filter alone could not remove these noises without removing part of the melt microstructure.

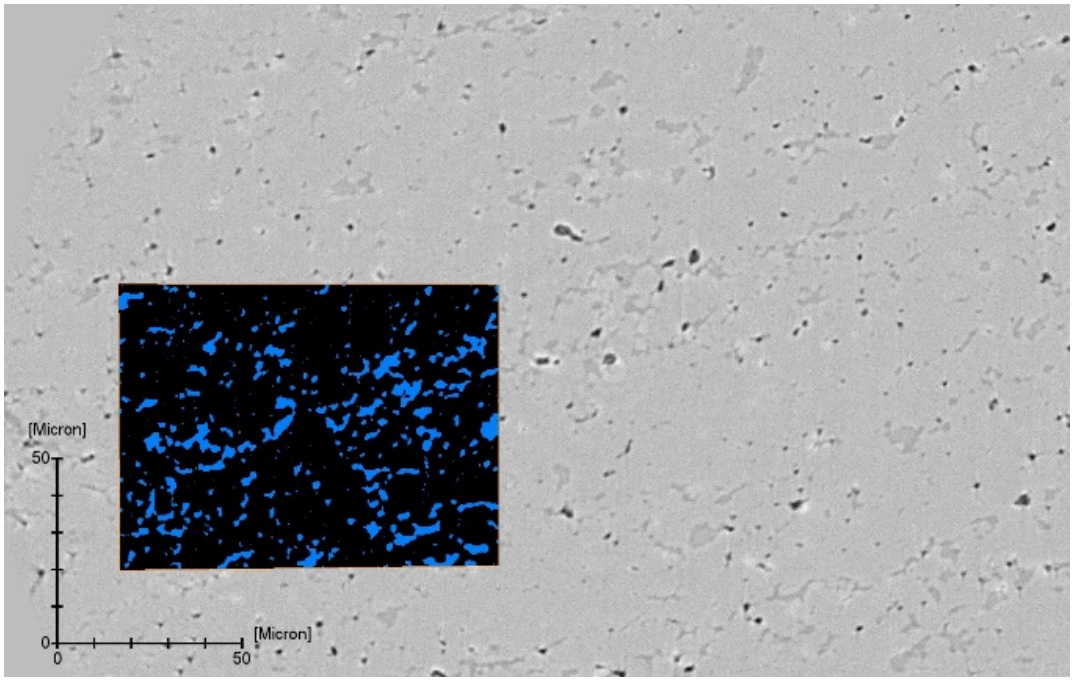

Figure 9: 2-D slice of the three-dimensional thresholded region, where the black represents solid (olivine), and the blue color denotes the pore space (occupied by basalt). This was produced by the *interactive thresholding* module, where the range of grayscale values that were visually observed as melt was selected.

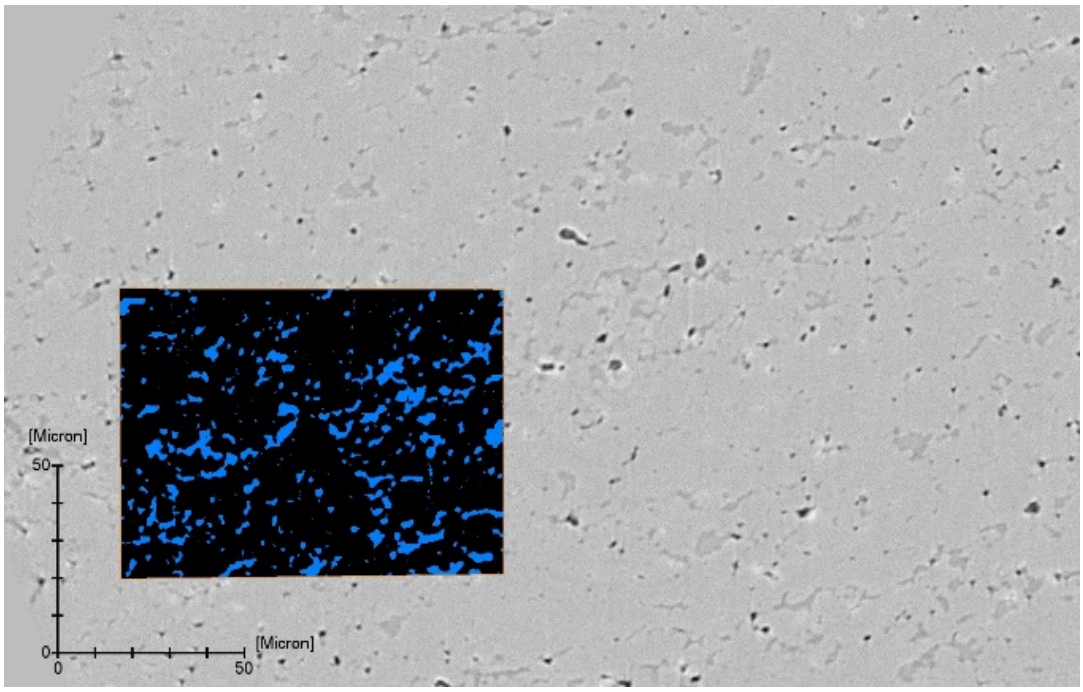

Figure 10: A final filter, *remove small spots*, was used to remove the final spots below 10 pixels in size. At this pixel size, the connectivity results were not affected, tested by measuring the connectivity sample-wide with and without using this module.

While the filtering techniques are shown within the black box in Figures 8-10, the image processing was applied to the entire 3D volume. The images have no noise that is particular to the region displayed, and so the subvolume shown is representative of the entire sample. Sample CQ0705 is roughly cylindrical. Figure 11 shows a coordination system SxSySz, where the S_Z axis is along the axial direction, and Sx and Sy are two orthogonal axes along the radial direction. Because all the calculations are done using Avizo, aligning the melt bands using the XYZ coordinates pre-defined by Avizo simplifies the characterization of anisotropy associated with melt bands. Therefore, sample CQ0705 was rotated 344º around the S_X axis, and 20º around the S_Z

axis (Figure 11). After sample rotation, the X and Z axes are along melt bands, and the Y axis is across melt bands (Figure 11).

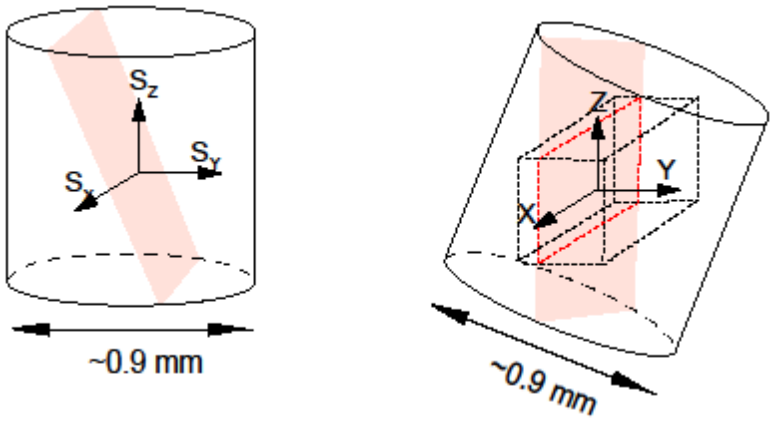

Figure 11: Rotation of sample CQ0705. After a rotation of 344º around the S_X axis, and 20º around the S_Z axis, the X and Z axes are along melt bands, and the Y axis is across melt bands.

2.3: Subvolume Selection

Subvolumes were selected throughout sample CQ0705 to obtain melt fraction, melt connectivity, and permeability. A compilation of the results for each subvolume analyzed is shown in Table 1. To keep the subvolume either entirely within a melt band, or outside a melt band, the subvolume width (ΔY) was constrained by the width of the melt band, 150 pixels (24 μm). The subvolume length (either ΔX or ΔZ dependent of the flow direction) along melt bands was 800 pixels (128 μm), which was chosen so that the subvolume would be representative of the region of interest. The side length of the third dimension of the rectangular subvolume (either ΔZ or ΔX), perpendicular to the flow direction along the melt bands, equals ΔY. The size of each subvolume is given as ΔXxΔYxΔZ.

In addition, flow simulations were conducted on subvolumes with an extended domain, 128x48x48 micron in size. In these simulations, the inlet and outlet of the fluid

flow are the same as in the simulations on subvolumes within a melt band. However, instead of having impermeable boundaries, these simulations permit flow meander out of the melt band and into the extended domain surrounding the subvolumes. The extended domain provides a solution to reduce the impact of the imposed impermeable boundaries on the permeability of the melt band. Finally, a large subvolume (128x128x128 μm^3) was analyzed to evaluate the permeability and melt connectivity of the sample as a whole. Figure 12 shows examples of a large subvolume at 128x128x128 μm^3 (the yellow box, Figure 12), a smaller subvolume at 128x24x24 μm^3 (the red box, Figure 12) and its corresponding extended domain (the green box, Figure 12). Subvolumes were also selected in the melt poor regions to understand permeability and connectivity within these regions.

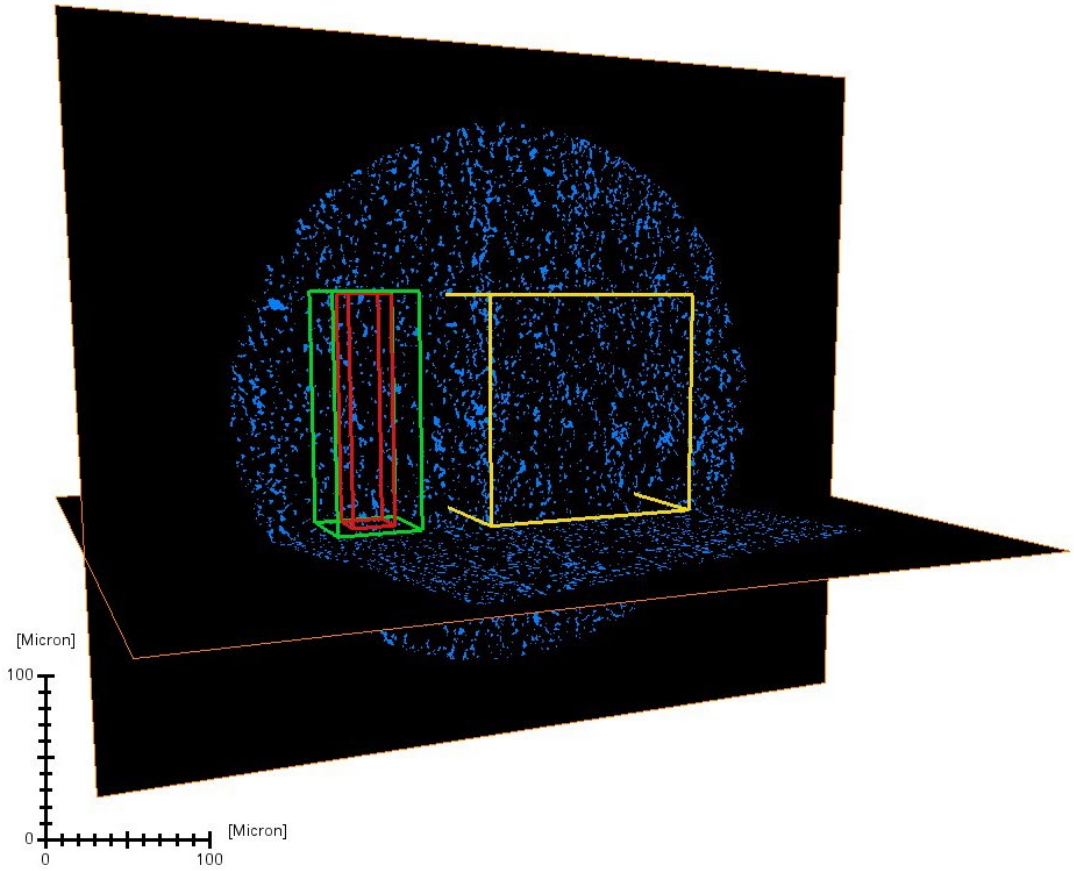

Figure 12: Different subvolume configurations selected from the fully thresholded sample CQ0705. The subvolume in red is 128x24x24 μm^3. The green region represents subvolumes where the fluid inflow and outflow region is kept the size of the red subvolume, but the flow can meander outside this restricted region so long as it stays within the green extended subvolume. The yellow subvolume corresponds to the large subvolume discussed in the connectivity and permeability section, is 128x128x128 μm^3 in size and contains both melt poor and melt rich regions.

2.4: Melt Fraction

Melt fraction is measured from the 3D melt distribution using the *volume fraction* module in Avizo. The number of voxels assigned to melt in a region divided by the total number of voxels in this region, yields melt fraction. Several subvolumes

were selected both within melt bands and in the melt poor regions to determine melt distributions throughout the sample. The largest subvolume was selected to encompass as much of the sample as possible to determine the average melt fraction of the entire sample. As further explained in the next section, how much of the melt matrix is connected can be determined by measuring the connected melt fraction versus the total melt fraction.

2.5: Melt Connectivity

Connectivity of the melt network was examined within melt bands, outside melt bands, and around the whole sample along X, Y and Z directions. The *axis connectivity* module within Avizo enables the evaluation of connected pore space in a subvolume. This module keeps the connected pore space by either a 6, 18, or 26 neighbor method (corresponding to just voxel faces, faces and edges, or faces edges and corners), between two parallel planes, which is defined in the X, Y, and Z directions. All results later discussed use the 6-neighbor method.

The connected melt fraction divided by the total melt fraction yields the percentage of pore space that is connected, and this data can be visualized using *volume rendering*. Melt connectivity was measured in subvolumes either entirely within melt bands or outside melt bands, constrained by parallel planes separated in either along-band and across-band directions, and in large subvolumes containing multiple melt bands.

2.6: Permeability

The permeability of each subvolume can be obtained using various methods. Avizo XLab Hydro offers two modules; one module is the *Absolute Permeability Tensorial Calculation* (APTC), which uses periodic boundary conditions to calculate the permeability tensor through volume averaging. When the APTC methods was used to calculate the permeability tensor, the flow simulations did not reach convergence after several weeks and had to be terminated. The software is not suitable for calculating permeability tensors of CQ0705, in which a significant portion of the flow paths are barely a few voxels.

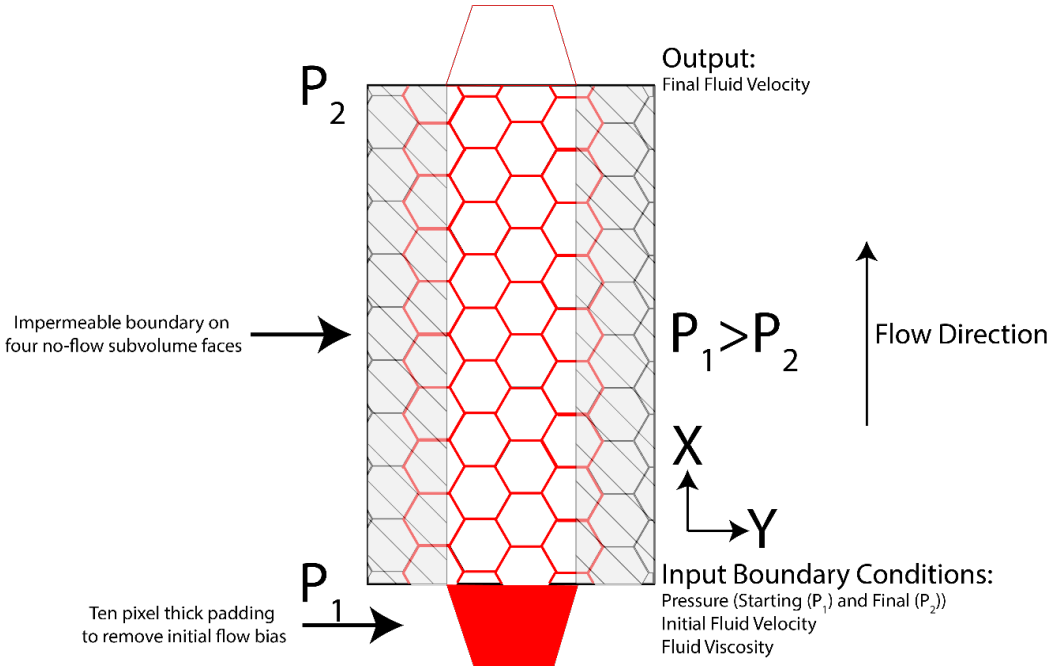

Figure 13: Conceptual diagram of the *absolute permeability experimental solution* (APES) in Avizo. Flow is initiated in the X direction by pressure gradient, with no flow in other directions by way of an impermeable boundary layer added to four of the six subvolume faces. The region is padded at the start and end to ensure there is no bias towards the large pore space in initial flow through the subvolume face.

The *Absolute Permeability Experimental Solution* (APES) method provide the permeability value for a given fluid flow direction. The APES calculates permeability in one direction by padding two parallel planes with a ten-pixel-thick highly porous inlet to remove initial flow bias, while keeping the other 4 planes of a subvolume impermeable by adding a one-voxel-thick panel of impermeable material. A pressure gradient is initiated, and a fluid flows through the digital pore space. The velocity field for the subvolume was calculated using Navier-Stokes equations. When a specified threshold of convergence is reached, the permeability of the subvolume is obtained using Darcy's law.

While the APES module does not provide the full tensor, for each subvolume, one can set up the pressure gradients to drive the fluid flow along X, Y, and Z directions and calculate K_X, K_Y, and K_Z respectively. The APES method was considered more representative of fluid flow in a geologic sense where fluid moves in response to a pressure gradient (Figure 12).

The impermeable boundaries imposed around the subvolumes can cause large scatters in the permeability values because the flow paths meander out the imposed impermeable boundaries would become dead-ends for flow even though some of them actually turn back in to the subvolume (Figure 13). To circumvent this problem, the APES simulations were repeated for the same subvolume with an extended domain that is larger than the inlet size (Figure 14) to allow melt flow meander in and out the artificially imposed boundaries of the original subvolume. These extended domain calculations take into consideration the tortuosity of the melt network (see section 3.3), and produced more consistent permeability results. Computation time for the APES

approached a month for the extended domain calculation, which severally limited the usefulness of this technique.

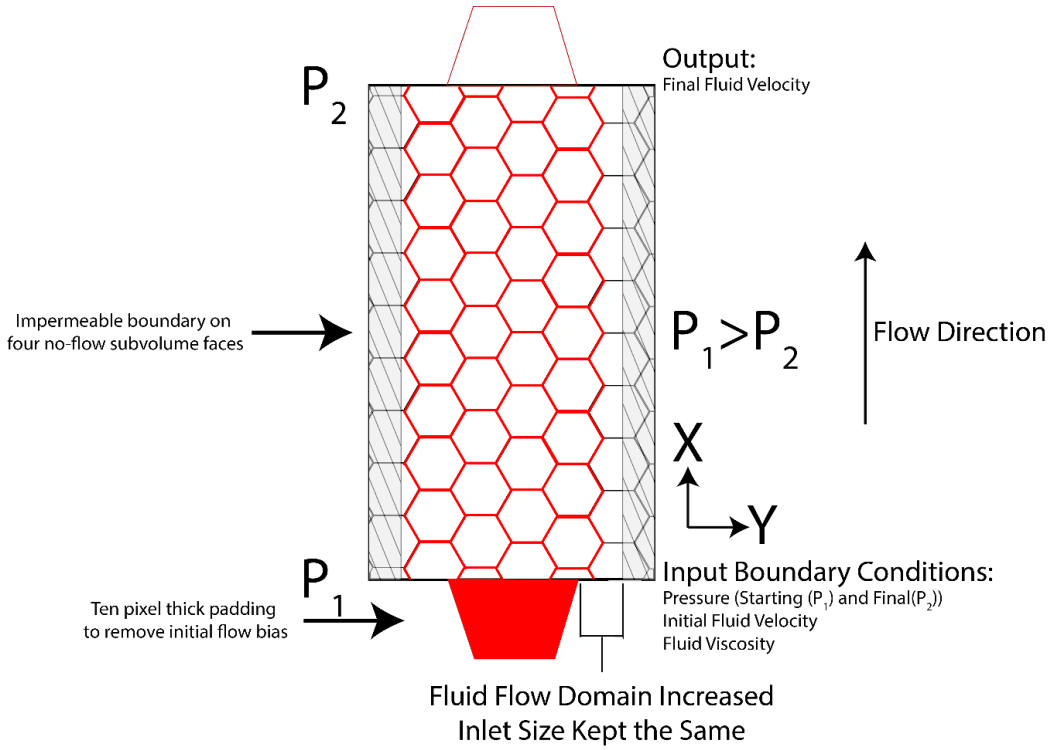

Figure 14: Calculation showing the APES using the extended domain subvolumes for permeability calculation. The inlet is kept the same while the domain is extended. This allows fluid flow paths that go outside the subvolume to be included in the flow field, so long as the fluid returns to the region between the inlet and outlet of the subvolume.

Permeability was calculated using another method when data variation and computation time was notably high. PerGeos ©ThermoFisher Scientific offers a *Lattice Boltzman Method (LBM)* module in contrast to the APES method offered in XLab Hydro. Lattice-Boltzmann methods are often more efficient for fluid-flow problems, especially in heterogeneous porous networks, largely because the lattice-Boltzmann

equations do not require inversion of a large matrix containing all the degrees of freedom in a numerical system (Chen & Doolen, 1998).

The LBM obtains macroscopic fluid velocity by averaging momentum of fluid particles along sites of a grid, or lattice (McNamara & Zanetti, 1988). By calculating the probability of the number of particles at a site, instead of the precise number of particles, and by using a grid instead of tracking each individual particle, computation time is significantly reduced. This method has proven to be effective in calculating permeability of porous rock (Boek & Venturoli (2009). These methods are shown to be specifically effective when considering complex porous networks, as found by Bernsdorf et al. (1999).The permeability results presented for CQ0705 rely mostly on this method.

2.7: Grain Size Quantification through Electron Backscatter Diffraction

Permeability is dependent on grain size (eqn. 1). To extrapolate experimentally constrained permeability values to Earth's mantle, the grain size of experimental charges must be obtained. Because X-ray synchrotron microtomography is not able to detect the contacts between olivine grains due to the lack of adsorption contrast, electron backscatter diffraction data was used to obtain grain size of CQ0705.

Electron backscatter diffraction (EBSD) is a useful method to detect grain boundaries in rocks (Qi et al., 2015; 2018). EBSD works by using an electron source to bounce electrons of a sample surface tilted at 70°. The diffraction pattern of these electrons are recorded by a detector, allowing for a per-pixel estimate of orientation of a grain or compound (Figure A1). EBSD is typically used for rigorous analysis of, for example, grain orientation or to understand mineral physics. Here, I use EBSD to

delineate grains and determine the grain size of the experimentally deformed samples. Data was collected in Qi et al. (2015, 2018) by mechanically polishing the rock sample before imaging a region using procedures outlined in Hansen et al. (2011), with grain size reconstruction and quantification taking place in MTEX (Bachmann et al., 2010).

MTEX allows for electron backscatter diffraction data to be imported and quantified in Matlab. There are several commands that allow for grain boundaries to be drawn based on the difference in orientations between pixels with an orientation threshold specified by the user. By lumping pixels with similar crystallographic orientations and drawing boundaries when pixels are different above the orientation angle set by the user, grains are constructed. Then, grain diameters can be measured within MTEX allowing for grain-size averaging.

Chapter 3: Results

3.1: Melt Distribution

The melt fraction of the large subvolume (200x200x200μm), which encompasses approximately the whole sample, is 0.109. This value is used as the average melt fraction of CQ0705. Figure 15 reports the melt fractions of 23 subvolumes (128x24x24 μm^3), taken either entirely within a melt band, or completely outside melt bands, in dimensions. Melt fraction in these subvolumes ranges from 0.078 to 0.178.

Melt fraction is bimodal, with subvolumes outside the melt band having melt fraction lower than the sample average. Subvolumes selected inside a melt band have a higher than average melt fraction. No subvolume inside or outside the melt band has the sample average. The subvolume with the highest melt fraction has a melt fraction 2.6 times greater than the subvolume with the lowest melt fraction. The subvolume with the highest melt fraction has a melt fraction 1.6 times greater than the average, while the subvolume with the lowest melt fraction has a melt fraction 0.71 times the average.

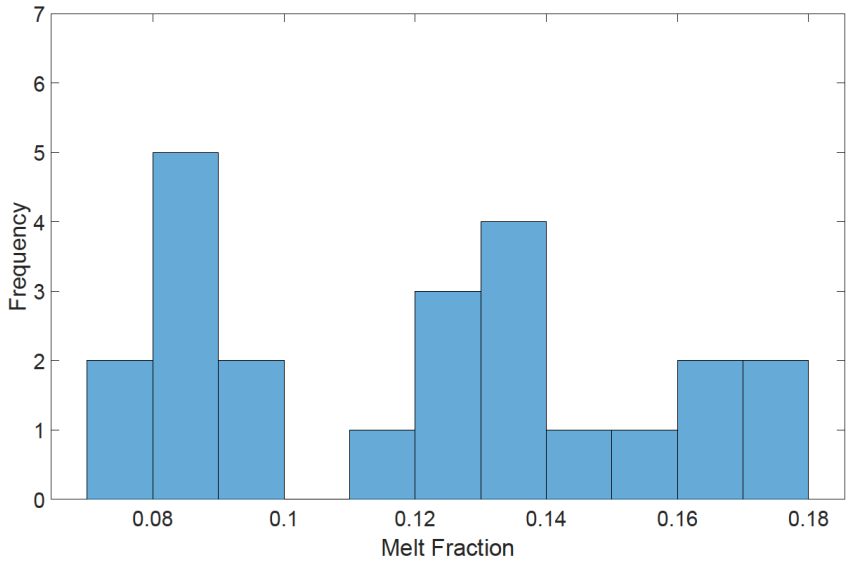

Figure 15: Histogram of melt fractions of 23 subvolumes. The size of each subvolumes is 128x24x24 μm^3. Which is taken either entirely within a melt band, or completely outside melt bands. Within melt bands, melt fraction ranges from 0.109 to 0.178. Outside melt bands, melt fraction ranges from 0.078 to 0.098.

3.2: Melt Connectivity

Melt is connected in both the X and Z directions through sample CQ0705. These were defined as the along-band direction by sample rotation, and correspond to visually observable melt enriched planar features. Regions in between these melt-rich bands are melt poor and disconnected in all three directions, though as seen in Figure 16, on small length scales outside of the melt band, there may be some connectivity.

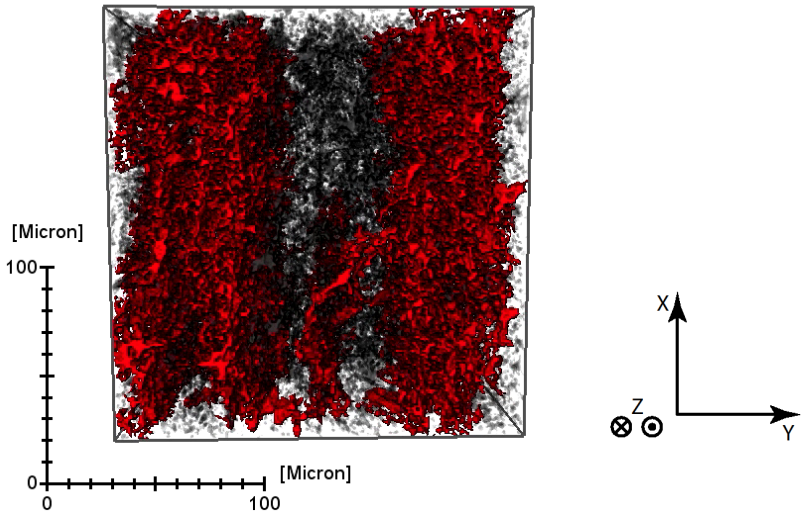

Figure 16: Subvolume 128x128x128 μm in size, with connected pore space in the X direction shown in red, and disconnected pore space shown in gray. The connected regions in red are the planar melt-rich bands, and the gray regions in between are the melt poor region where there is little to no connectivity found.

Melt is connected within the melt bands found in sample CQ0705, in all three directions (Figure 17).

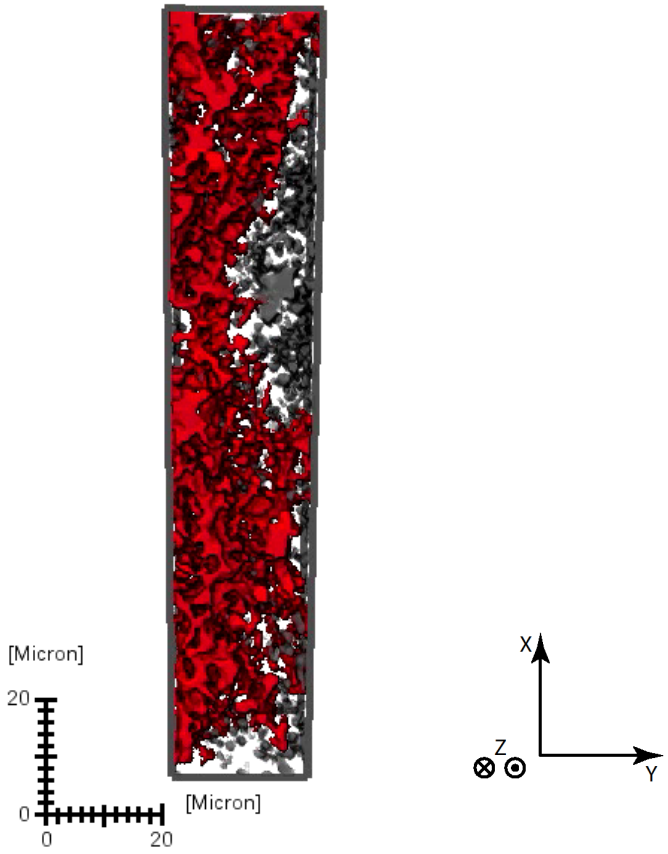

Figure 17: Subvolume taken within a melt band, 128x24x24 μm in size. The connected pore-space is shown in red, and the disconnected pore space in gray.

In the melt poor regions, there is no connectivity, in any directions, along-band or across-band (Figure 18). When examining the entire sample, or a large subvolume that contains both melt bands and melt-poor regions, melt is connected only in the along-band direction. There is no connectivity across-band on a large scale, due to the lack of melt connectivity in the melt-poor regions (Figures 16, 18).

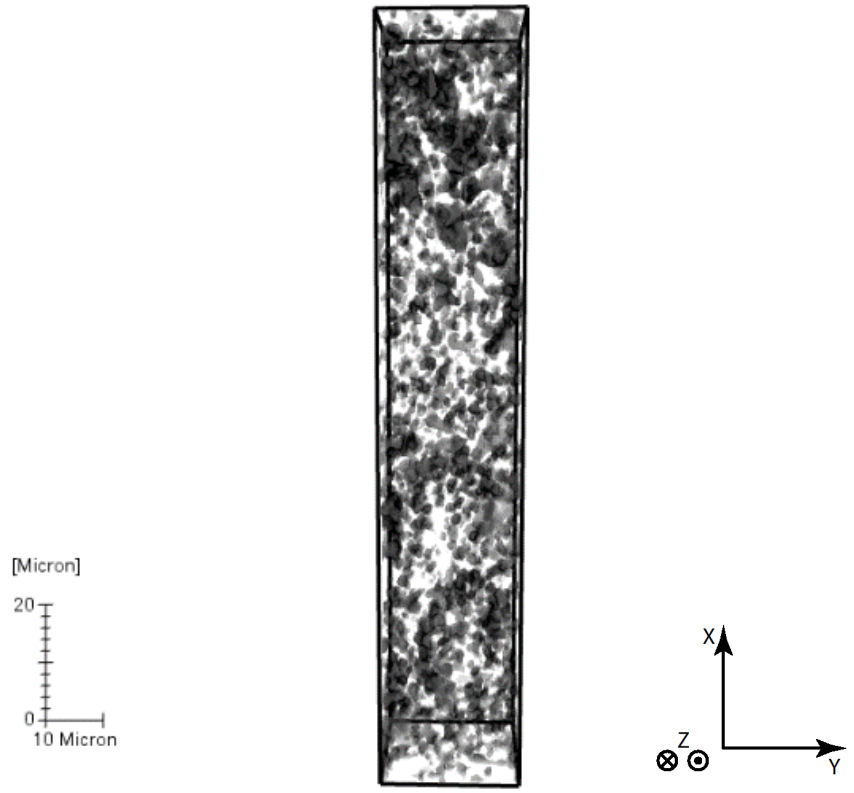

Figure 18: Subvolume taken outside of a melt band, 128x24x24 μm in size. All pore space is disconnected, shown in gray. This pore space is disconnected in the X, Y, and Z direction.

Figure 19 shows how the connected melt fraction is correlated with total melt fraction for different subvolumes. The measurement shown reports connectivity in either the X or Z direction, both inside and outside the melt band. Subvolumes with melt fraction above the sample average have connected melt fractions that range between 65% and 90% of that subvolumes total melt fraction. Subvolumes with melt fraction below the average melt fraction have no connectivity. A large subvolume containing both melt-rich bands and melt poor matrix is shown as a black square and has half its pore space connected (the gray subvolume in Figure 11). Above the sample average, inside the melt band, melt is connected, and can be constrained by a linear

relationship. Connected melt fraction (ϕ_c) is proportional to melt fraction (ϕ), where $\phi_c = 1.2\phi - 0.6$.

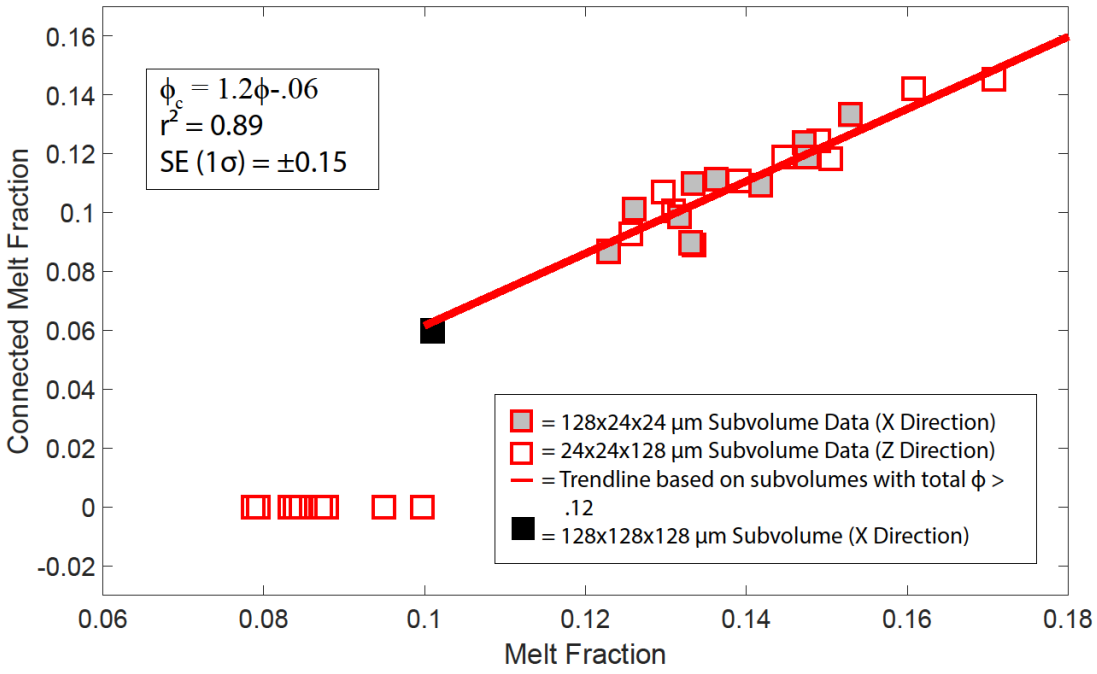

Figure 19: Graph showing melt fraction versus connected melt fraction for subvolumes taken throughout sample CQ0705. The gray-filled squares correspond to connected melt fraction for subvolumes 128 µm long in the Z direction, while the empty symbols correspond to connected melt fraction for subvolumes 128 µm long in the X direction. The black square represents a subvolume 128 µm long in each direction, which contains both melt poor and melt-rich regions (gray subvolume Figure 11). A trend line is shown for the subvolumes that have some connected melt, and are 128x24x24 μm^3 in dimension. They represent subvolumes inside the melt band.

3.3: Partial Melt Permeability

The APES permeability measurements are provided in Table 1, and were calculated in the X and Z direction. No results are presented in the Y direction for subvolumes as long as the X and Z direction, since there is no connected melt network in the Y direction for subvolumes 128 μm long. These measurements showed significant variation with subvolumes 128x24x24 μm like the red region in Figure 11. Two extended domain calculations were run for particularly anomalous regions, which showed higher permeability that reduced the spread in variation, however the computation time took approximately one-month each. Therefore, the LBM was used for both the 128x24x24 subvolumes and associated extended domain subvolumes. Even an extended domain calculation took less than 24 hours.

The issue of band planarity or melt network tortuosity is evident in the 3D flow field (Figure 20), which are an output of the APES method. Figure 20 shows the flow field for both the 128x24x24 μm^3 subvolume and the same subvolume with an extended domain. The extended domain simulations include flow that would be cut off in the subvolume calculations.

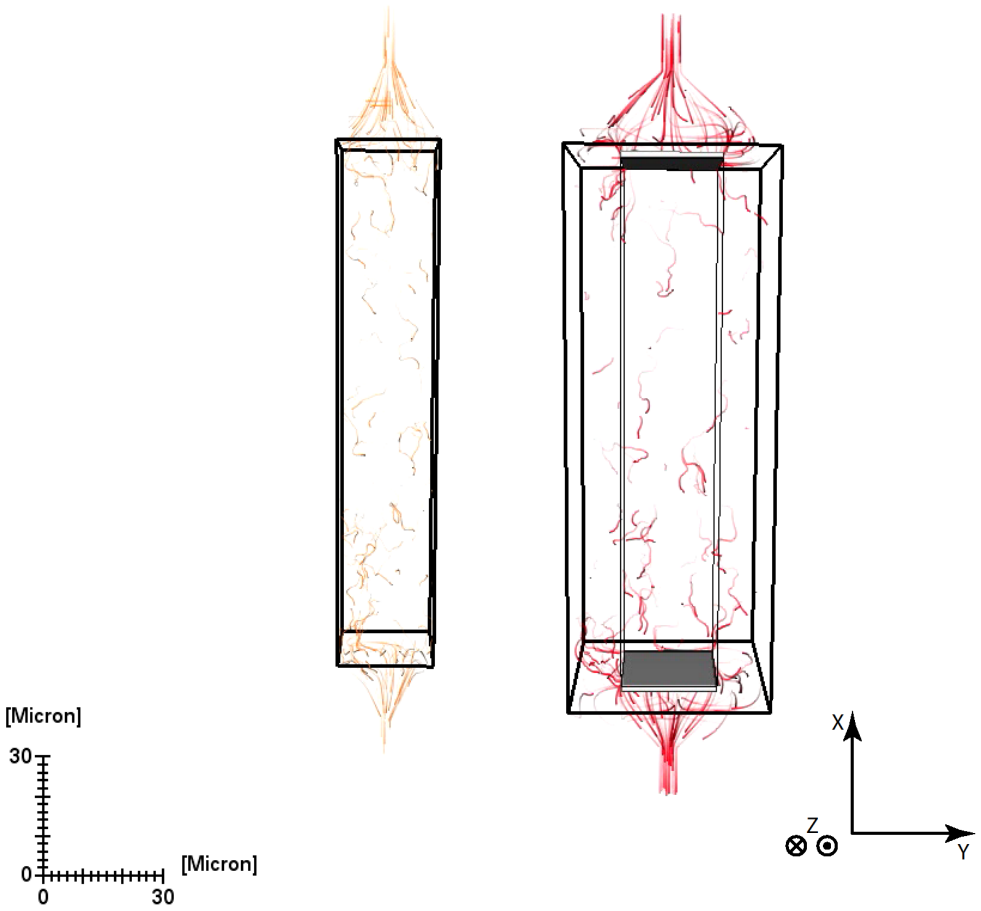

Figure 20: Image of two flowpath animations, produced by the APES velocity field in Avizo. The yellow flowlines denote fluid flow at a point in time through the 128x24x24 subvolume, while the right subvolume is the same region with an extended domain permitted for fluid flow. The axis are notated, with the long axis of calculation in the X direction.

Figure 21 shows LBM permeability results for the X direction for subvolumes within the melt band and associated extended domain calculations. The extended domain calculations can be fit using a similar power-law relationship like that in Miller et al., 2014, where permeability is proportional to melt fraction raised to a power-law exponent (equation 1). The power-law exponent for the extended domain subvolumes is 3.2±0.8, while it is 4.1±1.5 for the 128x24x24 subvolumes in the X direction. The

full equation 1 fitted to the extended subvolume data in the X direction is $k = \frac{\phi^{3.2} d^2}{12.4}$ and for the 128x24x24 subvolume data $k = \frac{\phi^{4.1} d^2}{6.5}$. Permeability is greater in the extended subvolume compared to its regular subvolume counterpart.

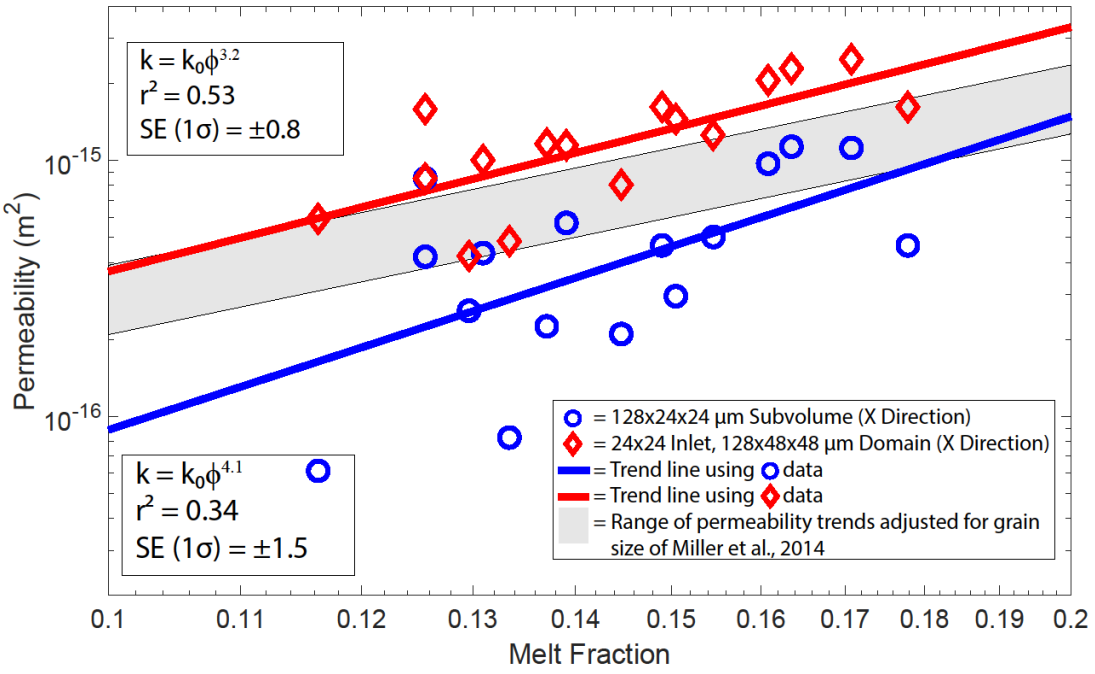

Figure 21: Permeability versus melt fraction in a log-log plot. Data was collected using the LBM. All data shown was collected in the X direction within sample CQ0705. The blue line shows trend fitted to the regular subvolumes (circle symbols), while the red is for the extended domain calculations (diamond symbols).

Permeability results are not shown for regions outside melt-rich bands, as there is no connectivity, and as such, permeability is zero. Permeability is also not shown for directions across-band, as on all length scales greater than the width of the melt band, there is no connected melt fraction. There could exist small connections below the image resolution, though permeability based on these small connections would be much less than the detectable permeability. If grain size is equal to or less than the

image resolution (0.16 μm), and $k \propto d^2$, then the undetected permeability would be at least ~260 times less than the observed permeability, going from the observed grain size of 2.6 μm to the unobserved image resolution grain size of 0.16 μm. At the lowest melt fraction, with a measured permeability of $2.4 \times 10^{-16} m^2$, the permeability with a grain size approaching the image resolution would then be near $0.9 \times 10^{-19} m^2$, or even lower.

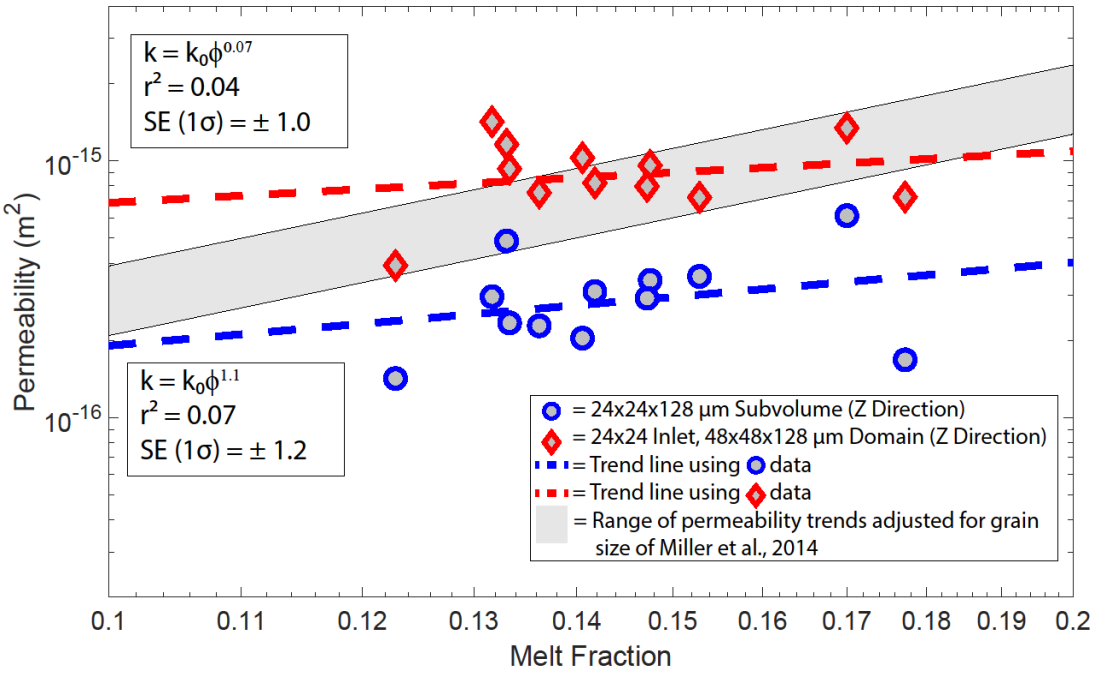

Figure 22: Permeability versus melt fraction in a log-log plot. These data show permeability results for the other along-band direction, the Z direction, where extended domain subvolume data is shown with red diamonds filled in gray, fitted by a dashed red line, and 24x24x128 μm^3 subvolume data denoted by blue circles fit by a dashed blue line.

Melt permeability results were collected for the Z direction as well (Figure 22). This direction is along-band , like the X direction, as the bands are planar. Melt permeability results are similar between the X and Z direction, considering the variation

seen within each direction. However, the Z direction are more scattered than measurements along the x-direction. When using a line of best fit and equation one, the Z data equation is $k = \frac{\phi^{1.1} d^2}{2967}$ (power law exponent of 1.1±1.0). The extended subvolume data equation is $k = \frac{\phi^{0.07} d^2}{2111}$ (Figure 22). Extended domain calculations in both directions show more consistency than their narrower subvolume counterparts.

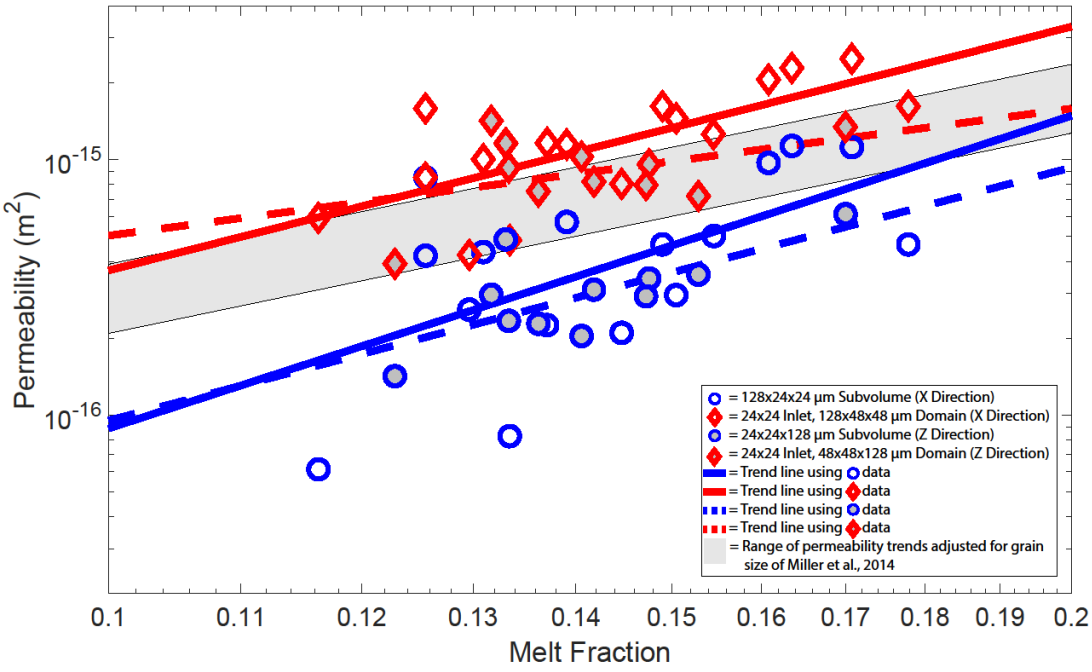

Figure 23: Summary log-log plot including all permeability versus porosity calculations for CQ0705 using the LBM, in both along-band directions.

ϕ	ϕ_{cX}	ϕ_{cY}	ϕ_{cZ}	X_0	Y_0	Z_0	ΔX	ΔY	ΔZ	Kx	Ky	Kz	Method	Extended Domain	Inside/ Outside bands	ID
0.178							800	100	150	8.0E-04	5.0E-04	1.9E-03	APES	N	Inside	1
0.178	0.160	0.160	0.160	1200	1350	1875	800	150	150	5.8E-04	3.9E-04	1.6E-03	APES	N	Inside	1
0.178				1200	1275	1800	800	300	300	4.1E-04			LBM	Y	Inside	1
0.178	0.160	0.160	0.160	1200	1350	1875	800	150	150	4.7E-04			LBM	N	Inside	1
0.177	0.157	0.157	0.157	1200	1385	700	150	150	800			1.7E-04	LBM	N	Inside	2
0.177				1125	1310	700	300	300	800			1.8E-04	LBM	Y	Inside	2
0.177	0.157	0.157	0.157	1200	1385	700	150	150	800			3.1E-04	APES	N	Inside	2
0.171	0.145	0.145	0.145	400	1350	1200	800	150	150	1.3E-03	8.6E-05	1.5E-03	APES	N	Inside	3
0.170	0.152	0.152	0.152	400	1375	1225	150	150	800			6.1E-04	LBM	N	Inside	4
0.170				325	1300	1225	300	300	800			3.4E-04	LBM	Y	Inside	4
0.170	0.152	0.152	0.152	400	1375	1225	150	150	800			7.9E-04	APES	N	Inside	4
0.164				1200	800	1275	800	300	300	5.7E-04			LBM	Y	Inside	5
0.164	0.141	0.141	0.141	1200	875	1350	800	150	150	1.1E-03			LBM	N	Inside	5
0.161				1400	1400	2200	800	150	150	9.7E-04			LBM	N	Inside	6
0.161				1400	1325	2125	800	300	300	5.1E-04			LBM	Y	Inside	6
0.161	0.142	0.142	0.142	1400	1400	2200	800	150	150	1.2E-03	1.9E-04	1.7E-03	APES	N	Inside	6
0.155							800	150	150	5.0E-04			LBM	N	Inside	7
0.155							800	300	300	3.2E-04			LBM	Y	Inside	7
0.153	0.133	0.133	0.133	1000	1400	1200	150	150	800			4.1E-04	LBM	N	Inside	8
0.153	0.133	0.133	0.133	1000	1400	1200	150	150	800			3.6E-04	APES	N	Inside	8
0.153				1000	1325	1125	300	300	800			1.8E-04	LBM	Y	Inside	8

0.153				700	1325	1375	800	300	300	3.2E-04			LBM	Y	Inside	9
0.153	0.129	0.129	0.129	700	1400	1450	800	150	150	5.0E-04			LBM	N	Inside	9
0.150				1100	1300	650	800	300	300	3.6E-04			LBM	Y	Inside	10
0.150	0.118	0.118	0.123	1100	1375	725	800	150	150	2.9E-04			LBM	N	Inside	10
0.150	0.118	0.118	0.123	1100	1375	725	800	150	150	2.7E-04	1.4E-04	6.7E-04	APES	N	Inside	10
0.149				1200	1275	1800	800	300	300	4.1E-04			LBM	Y	Inside	11
0.149	0.124	0.124	0.124	1200	1350	1875	800	150	150	4.7E-04			LBM	N	Inside	11
0.148	0.119	0.119	0.119	1600	850	600	150	150	800			3.4E-04	LBM	N	Inside	12
0.148				1525	775	600	300	300	800			2.4E-04	LBM	Y	Inside	12
0.147	0.124	0.124	0.124	1725	850	1000	150	150	800			2.9E-04	LBM	N	Inside	13
0.147				1650	775	1000	300	300	800			2.0E-04	LBM	Y	Inside	13
0.146	0.124	0.124	0.124	1250	850	825	800	150	150	8.2E-04			APES	N	Inside	14
0.145				475	1825	600	800	300	300	2.0E-04			LBM	Y	Inside	15
0.145	0.119	0.119	0.119	550	1900	600	800	150	150	2.1E-04			LBM	N	Inside	15
0.145	0.119	0.119	0.119	550	1900	600	800	150	150	2.3E-04	1.1E-04		APES	N	Inside	15
0.142	0.109	0.109	0.109	2000	1350	600	150	150	800			3.1E-04	LBM	N	Inside	16
0.142				1925	1275	600	300	300	800			2.0E-04	LBM	Y	Inside	16
0.141	0.104	0.104	0.104	1650	1400	800	150	150	800			2.0E-04	LBM	N	Inside	17
0.141				1575	1325	800	300	300	800			2.6E-04	LBM	Y	Inside	17
0.141	0.104	0.104	0.104	1650	1400	800	150	150	800			6.8E-05	APES	N	Inside	17
0.139				1000	1875	1125	800	300	300	2.9E-04			LBM	Y	Inside	18
0.139	0.111	0.111	0.111	1000	1950	1200	800	150	150	5.7E-04			LBM	N	Inside	18
0.139	0.111	0.111	0.111	1000	1950	1200	800	150	150	8.3E-04	1.3E-04	9.2E-04	APES	N	Inside	18
0.137				600	1900	625	800	150	150	2.2E-04			LBM	N	Inside	19
0.137				600	1825	550	800	300	300	2.9E-04			LBM	Y	Inside	19
0.137	0.108	0.108	0.108	600	1900	625	800	150	150	1.9E-04			APES	N	Inside	19

0.136				1400	1825	1400	300	300	800			1.9E-04	LBM	Y	Inside	20
0.136	0.111	0.111	0.111	1475	1900	1400	150	150	800			2.3E-04	LBM	N	Inside	20
0.133	0.089	0.089	0.089	900	775	1425	800	300	300	1.6E-04			APES	Y	Inside	21
0.133				900	850	1500	800	150	150	8.3E-05			LBM	N	Inside	21
0.133				900	775	1425	800	300	300	1.2E-04			LBM	Y	Inside	21
0.133	0.089			900	850	1500	800	150	150	6.4E-05	5.6E-05		APES	N	Inside	21
0.133				875	1875	575	300	300	800			2.3E-04	LBM	Y	Inside	22
0.133	0.110	0.110	0.110	950	1950	575	150	150	800			2.3E-04	LBM	N	Inside	22
0.133				950	1950	575	150	150	800			1.7E-04	APES	N	Inside	22
0.133				725	1700	1000	300	300	800			2.9E-04	LBM	Y	Inside	23
0.133	0.090	0.079	0.079	800	1775	1000	150	150	800			4.9E-04	LBM	N	Inside	23
0.132				625	1300	900	300	300	800			3.6E-04	LBM	Y	Inside	24
0.132	0.099	0.099	0.099	700	1375	900	150	150	800			3.0E-04	LBM	N	Inside	24
0.131				1000	1800	1525	800	300	300	2.5E-04			LBM	Y	Inside	25
0.131	0.101	0.101	0.101	1000	1875	1600	800	150	150	4.3E-04			LBM	N	Inside	25
0.131	0.101	0.101	0.101	1000	1875	1600	800	150	150	4.1E-04	3.0E-05	7.6E-04	APES	N	Inside	25
0.130				1125	800	1350	800	300	300	1.1E-04			LBM	Y	Inside	26
0.130	0.107	0.107	0.107	1200	875	1350	800	150	150	2.6E-04			LBM	N	Inside	26
0.130	0.107	0.107	0.107	1200	875	1350	800	150	150	2.4E-04			APES	N	Inside	26
0.126				1400	1325	2125	800	300	300	5.2E-04			APES	Y	Inside	27
0.126				725	950	2000	800	300	300	2.1E-04			LBM	Y	Inside	28
0.126	0.093	0.093	0.093	800	1025	2000	800	150	150	4.2E-04			LBM	N	Inside	28
0.126	0.093	0.093	0.093	800	1025	2000	800	150	150	4.1E-04	6.8E-05		APES	N	Inside	28
0.126				925	725	925	800	300	300	4.0E-04			LBM	Y	Inside	29
0.126				925	800	1000	800	150	150	8.5E-04			LBM	N	Inside	29
0.126	0.082	0.082	0.082	925	800	1000	800	150	150	1.0E-04			APES	N	Inside	29

0.123				1225	775	800	300	300	800			9.8E-05	LBM	Y	Inside	30
0.123	0.084	0.084	0.084	1300	850	800	150	150	800			1.4E-04	LBM	N	Inside	30
0.123	0.084	0.084	0.084	1300	850	800	150	150	800			1.4E-04	APES	N	Inside	30
0.116				800	2075	1500	800	300	300	1.5E-04			LBM	Y	Inside	31
0.116				800	2150	1575	800	150	150	6.1E-05			LBM	N	Inside	31
0.116				800	2150	1575	800	150	150	1.7E-04	1.2E-06		APES	N	Inside	31
0.101	0.060	0.060	0.060	1000	1700	1500	800	800	800	2.0E-04			LBM	N	Both	32
0.100	0.000	0.000	0.028	1200	1050	750	800	150	150						Outside	33
0.095	0.000	0.000	0.012	1100	1575	725	800	150	150						Outside	34
0.088	0.000	0.000	0.000	800	1150	1550	800	150	150						Outside	35
0.087	0.000	0.000	0.030	800	1550	1750	800	150	150						Outside	36
0.085	0.000	0.000	0.029				800	150	150						Outside	37
0.084	0.000	0.000	0.010	800	1625	900	800	150	150						Outside	38
0.083	0.000	0.000	0.009	800	1075	1200	800	150	150						Outside	39
0.079	0.000	0.000	0.000	800	1150	1700	800	150	150						Outside	40
0.079	0.000	0.000	0.000	800	1075	900	800	150	150						Outside	41

Table 1: A compilation of melt fraction (ϕ), connected melt fraction (ϕ_{cX}, ϕ_{cY}, ϕ_{cZ}) and permeability (K_X, K_Y, K_Z) along X, Y, Z directions of all subvolumes analyzed. The position of the lower left corner (X_0, Y_0, Z_0) and the side lengths (ΔX, ΔY, ΔZ) of the rectangular subvolumes are given in pixels. Methods used to calculate permeability were specified: APES represents the *absolute permeability experimental solution* in Avizo XLab Hydro and LBM represents the *lattice Boltzmann method* from PerGeos. Whether an extended domain was included in permeability simulation and whether the subvolume is inside or outside melt bands are marked. Subvolume ID that is unique to each 128x24x24 or 24x24x128 μm^3 subvolume is assigned to help identify equivalent calculations made using different methods.

3.4: Grain Size

It is important to quantify the grain size of sample CQ0705 since permeability is dependent on grain size squared (eqn. 1). As the formation of shear bands is related to the compaction length, Sample CQ0705 was designed to have small grain sizes (i.e., a few microns) to ensure melt band development within the experimental charge. For comparison, the typical grain size of a mantle rock is in the millimeter range.

Grain size as determined by electron-backscatter diffraction (EBSD), depends on the treatment of non-indexed points. Qi et al. (2018) provides grain size of PT0705 from which sample CQ0705 in this study was taken. However, the grain size of PT0705 provided by Qi et al. (2018) is not accurate enough for the melt-rich bands in sample CQ0705, as the former encompasses much larger regions.

Region	Treatment	Grain Size Mean	Grain Size Median	Grain Size (Average from histogram fit)	Indexed %
Outside Band 1	8	2.61	2.76	2.75	91.37
Outside Band 1	7	2.57	2.75	2.76	92.86
Outside Band 1	6	2.66	2.83	2.93	96.16
Outside Band 1	5	2.79	3.02	3.08	99.44
Inside Band 1	8	2.11	2.19	2.28	77.57
Inside Band 1	7	2.09	2.26	2.29	79.49
Inside Band 1	6	2.14	2.39	2.48	86.44
Inside Band 1	5	2.35	2.64	2.72	97.43
Inside Band 2	8	2.07	2.14	2.15	79.94
Inside Band 2	7	2.03	2.08	2.15	81.85
Inside Band 2	6	2.14	2.18	2.28	88.50
Inside Band 2	5	2.29	2.47	2.58	98.14
Inside Band 3	8	2.18	2.29	2.43	79.78
Inside Band 3	7	2.17	2.37	2.48	81.67

Table 2: Grain size estimates, in micron, for several regions of data obtained from Qi et al., 2018. Regions are labeled “inside band” and “outside band” as determined by planar regions with large numbers of non-indexed pixels, representative of non-crystalline material (melt).

The EBSD map obtained by Qi et al. (2018) was reanalyzed in this study. Special attention was paid to the non-indexed points in the EBSD data. The non-indexed points are pixels that are not identified as minerals. They may result from poor

data collection, or they could be melt, which is not crystalline. Melt fraction results presented here and experimental setup suggests melt fraction should be ~0.1. If all pixels are indexed, pixels that are melt would be assigned to a nearby grain. Therefore, indexing should not be greater than 90%, leaving at least the 10% that is melt unindexed. Furthermore, the assignment of pixels would be more pronounced near melt-rich bands, which, as discussed in sections 3.3 and 4.3, is where most of the melt flow would occur.

This creates substantial uncertainty in grain size estimate, especially in personal electron-backscatter work done on the sample imaged through X-ray microtomography. However, given the range of grain size averages when examining across treatments (Table 2), the grain size with the melt bands is most certainly between 2.2 and 2.8 μm. While assigning more pixels an index value of the local average, the EBSD data can yield a grain size of ~3 μm within the melt band. However, the index % of pixels approach 100%. As no more than 90% of pixels should be indexed, based on the presence of about 10% melt in the sample, this level of processing is considered unrealistic. Visualizations of the collected and treated electron backscatter diffraction imagery and grain size reconstruction are shown in the appendix.

Chapter 4: Discussion

4.1: Melt Connectivity and Melt Distribution

Melt segregation results show the regions inside visually identified melt bands have a higher-than-sample-average melt fraction. The corresponding matrix in between these melt bands has a lower-than-sample-average melt fraction. This is in agreement with 2D analysis of melt bands that develop from shear strain (Holtzman et al., 2003, King et al., 2010). The most melt rich subvolume, isolated within the band, is 1.6 times the sample average, a measurement discussed as the maximum normalized melt fraction in Holtzman et al. (2003), with the most melt poor region of the matrix is 0.72 times the sample average, a measurement discussed as a minimum normalized melt fraction in Holtzman et al. (2003). It could be expected that, at high strain as in sample CQ0705, melt-rich bands would have a melt fraction of 1.6 times the local average and the matrix would have a melt fraction of 0.5 times the local average. The maximum normalized melt fraction here (1.6) agrees with literature (Qi et al., 2015) which found a normalized maximum melt fraction of 1.6, with lower values seen for less strain. The minimum 3D normalized melt fraction observed here, of 0.72, is less than that observed by Qi et al (2015) who observed normalized melt fraction only as low as 0.8. The highest melt fraction observed is 2.25 times greater than the lowest, which shows a larger ratio than reported in Qi et al. (2015).

The 3D melt connectivity results presented here are starkly different from 2D results. King et al., 2010 assumed an outside-the-band permeability larger than 0, which is not supported by the lack of 3D connectivity observed here. King et al. (2010)

describes this assumption is made to explain the movement of melt into the melt-rich bands. However, while most regions in between the melt bands were found to have no connectivity, Figure 16 shows that connectivity may exist between melt bands on a small scale. It is also possible that there are small pore space connections below the limit of the imaging technique that could permit very minor amounts of flow between melt bands. Further work would be needed to explore this, possibly beyond current experimental and imaging limitations. The lack of connectivity is contrary to what is expected in a partially molten rock at textual equilibrium (von Bargen and Waff, 1986). Miller et al. (2014) found that the melt network in undeformed partially molten rocks remain fully connected for melt fractions as low as 0.01. This indicates that the sheared sample is not in textural equilibrium. This is likely resulted from a combination of the short duration of hot-pressing and the presence of mechanical deformation.

Melt is connected along-band but disconnected across-band in subvolumes that include multiple melt bands and regions of material outside the melt bands. As the sample was rotated so that the melt band is orthogonal to the axis system defined in Avizo, X and Z are along-band, and Y is across-band. Within melt bands, there is connectivity in all directions. However, across the entire sample, there is no 3D connectivity across-band, but there is connectivity along-band. In the melt poor regions, melt is entirely disconnected on the subvolume scale. This would indicate that when a partially molten rock is subjected to high degrees of shear strain similar to sample CQ0705, melt flow is restricted to the direction of the melt band orientation, within the melt bands.

These connectivity results have further implications for mid-ocean ridge magma transport. As it has been modeled by and others, given melt band orientation defined from the assumed stress field of a mid ocean ridge setting, melt flow would occur towards the mid ocean ridge axis towards the crustal surface. To understand this lack of connectivity and its implications, work remains to model the development of melt bands over time, as sample CQ0705 represents only one moment of time. In contrast, the deforming mantle beneath a mid ocean ridge changes over time. Therefore, melt bands may rotate and move as waves as described in King et al. (2010). It could also be that, over a longer length scale, the bands could turn into each other and are not entirely planar, enabling flow between bands described in King et al. (2010). Within sample CQ0705, the bands are parallel to each other, which reduces melt transport across bands.

4.2: Partial Melt Permeability

The LBM data provides the most consistent results, expected for heterogeneous pore networks (e.g., Boek & Venturoli, 2010), and is loosely constrained by the equation $k = \frac{\phi^{4.1} d^2}{6.5}$ when considering the 128x24x24 μm^3 subvolumes. The extended domain calculations allow the flow to meander outside of the narrow inlet and for the X direction, capture more of the variance within the power-law relationship expected between melt fraction and permeability. The extended domain calculations show less variance at a single melt fraction than the regions restricted to flow only between the 24x24 inlet. The extended domain permeability data in the X direction is better constrained, with a power-law relationship (equation 1) where $k = \frac{\phi^{3.2} d^2}{12.4}$. This data is

regarded as more geologically relevant where in nature flow is not restricted to a narrow subvolume but instead can extend over a larger area. This power-law relationship is similar to the proposed relationship in a heterogeneous, fractured melt network, but within one sigma uncertainty is indistinguishable for the undeformed melt network constrained by Miller et al. (2014). This could be due to the limited range of melt fractions observed in sample CQ0705, and the heterogeneity in melt network connectivity.

These results suggest that, for an olivine-basalt partially molten system, the permeability of regions outside melt-rich bands is negligible. Within melt-rich bands, the permeability is dependent on melt fraction with a power-law exponent n of 3.2, a value higher than that in an undeformed partially molten rock (n~2.6, Miller et al., 2014). The higher power-law exponent suggests that the connectivity of the melt network decreases with decreasing melt fractions (Zhu & Hirth, 2003).

The permeability of melt-rich bands is highly anisotropic, where the permeability component in the across-band direction is at least one order of magnitude lower than that along-band. The melt fraction-permeability relationship is complicated by the findings in the Z direction which is poorly constrained, though the dataset for this direction is smaller. When considering the error of the least squares regression model for the X direction where constraints are best, it is not certain the slope is higher than that of Miller et al. (2014), though this could be due to the limited range of melt fractions available in sample CQ0705.

The absolute values of permeability of the most melt-rich subvolumes are higher than in an undeformed partially molten aggregate like that in Miller et al. (2014),

though a better constraint on the error of the image analysis, perhaps using methods outlined in Miller et al. (2014), is necessary to demonstrate that these values are not in agreement. To provide better constraints on the power-law relationship and the absolute values of permeability shown here, studies that include a wider range of melt fractions, and examination of the melt pocket orientation between the Z and X direction presented in this study, could prove effective.

The anisotropy between the along-band and across-band direction observed in this study is significantly higher than the ~5-fold expected from Zimmerman et al. (1999). Along-band permeability is expected to be at least 260 times greater than across-band permeability, even if an undetected melt network exists below the image resolution. Table 1 shows that inside the band, the permeability across band is at least 80% less than the corresponding along-band permeability, and typically is 1-2 orders of magnitude less.

The complete lack of permeability outside of the melt bands could be due to the image resolution. A larger grain size would increase the melt pocket and melt tubule size. This could provide a more confident analysis of melt connectivity and permeability. However, grain size, which influences compaction length, is necessary to keep small in order to promote the development of melt bands on the sample size, as discussed in Holtzman et al. (2003). This is since the scale of melt band development is limited by the compaction length and sample size.

The range of melt fraction values is lower than that of the undeformed study presented by Miller et al. (2014). Samples with higher and lower initial melt fractions,

but similar strain and composition, could expand this range, which could provide a more complete quantification of the melt fraction-permeability relationship.

The olivine-basalt system is simpler than the mid-ocean ridge composition, where pyroxene is expected to be present. Zhu and Hirth (2003) noted that with significant amounts of orthopyroxene, there can be melt connectivity loss and the power law exponent increases from 2-3 as the melt network connectivity becomes heterogeneous. Miller et al. (2016) show that the power law exponent is ~2.6 in experimental samples that contained pyroxene proportions as much as 38%. As the power-law exponent in the X direction for CQ0705 is 3.2, the connectivity of this melt network changes considerably within the limited range of melt fractions (i.e., 0.101 to 0.176).

4.3: Mid-Ocean Ridge Implications

The results presented here have significant implications for melt transport at mid-ocean ridges. Given work that suggests melt bands induced by shear, like those quantified in this study, could orient towards the mid-ocean ridge axis when considering non-newtonian viscosity that best matches experimental melt band formation (Katz et al., 2006, Figure 3), the permeability anisotropy suggested here would indicate that melt flow would be much faster towards the ridge, along the melt bands, than across the melt bands. This characteristic would be particularly in regions close to the mid ocean ridge axis where shear strain is expected to be high. This is complicated however, by disagreement over melt shear band orientation in a mid-ocean ridge system, where Butler et al. (2009) found there could be a second set of melt shear band orientation, oriented sub-parallel to the base of the lithosphere, that would limit

the efficiency of melt transport towards the ridge, and melt could orient towards the base of the oceanic crust away from the ridge axis. However, neither of these studies include other methods of melt segregation or focusing, such as ridge suction (e.g., Sim et al. 2018), the reaction infiltration instability mechanism (e.g., Spiegelman et al. 2001), or a permeability barrier (e.g., Herbert & Montesi 2010).

The melt distribution results also suggest there could be no connectivity found in regions at high melt fractions, ranging from 0.079 to 0.100, with no permeability, unlike that in an undeformed partially molten aggregate, melt remains connected and permeable to melt fractions of 0.02 or potentially lower (Miller et al., 2014). However, this merits more study, as it could be an issue of scale as previously discussed, or there could be small melt connections not detected by the imaging technique. This could have implications for mid ocean ridge melt transport, where permeability outside melt bands would be significantly lower than within melt bands, despite having melt fractions only slightly less.

Even when connectivity is present (e.g., inside melt-rich bands, in the across-band direction in Table 1), permeability could still be lower perpendicular to the melt channel orientation, suggesting little melt movement perpendicular to the melt bands. The permeability anisotropy presented here could apply to other regions where channelization of melt is shown, with little melt movement perpendicular to the melt channel direction and focused flow in the direction of melt channels.

The exact values of permeability are likely not statistically different from the undeformed case in Miller et al. (2014), and the power law relationship is complicated, though the X direction along-band presented here offers the best constraint with the

equation $k = \frac{\phi^{3.2} d^2}{12.4}$. This could affect melt transport velocities when accounted for in numerical models. The results here also indicate that not all melt will be transported even when the system is permeable, where only 65-90% of the melt network was connected in sample CQ0705. This could have implications for melt retention.

Chapter 5: Conclusions

Using X-ray synchrotron microtomography and digital rock physics methods, 3D melt distribution of a sheared partially molten rock is obtained and analyzed. Within the melt-rich bands, melt fractions are above the sample average of 0.109, ranging from 0.116-0.178. Outside melt bands, melt fractions range from 0.076 to 0.095.

Melt is connected in every direction within the melt band. Outside of the melt band, there is little to no connectivity. Across the entire sample, there is no connectivity perpendicular to the melt band orientation. Inside the melt band, 65-90% of the total melt fraction is connected in each subvolume. The relationship between the connected melt fraction ϕ_c and the total melt fraction ϕ can be expressed as $\phi_c = 1.2\phi - 0.6$.

Due to the lack of melt connectivity, regions outside melt-rich bands are impermeable, despite having melt fraction up to 0.09. This results in no permeability across melt bands.

The simulation results using extended subvolumes show that the permeability of a melt-rich band along the X direction as function of melt fraction and grain size can be expressed as $k = \frac{\phi^{3.2} d^2}{12.4}$, with a power law exponent 3.2±0.8. The permeability along Z direction, $k = k_0 \phi^{1.1}$ with a power law exponent of 1.1±1.2, is less well constrained. The permeability in the Y direction within the melt band is at least an order of magnitude lower than that along the X or Z direction.

These results indicate that the permeability of a sheared partially molten rock is strongly anisotropic, with little to no flow occurs across the direction of melt band

orientation. The strong permeability anisotropy implies that formation of melt bands could be an efficient melt focusing mechanism at mid-ocean ridges.

Appendix

The filter tested iteratively assigns non-indexed pixels the value of nearby neighbors, and is discussed in depth by Hansen et al. (2011). 8 would represent the lowest treatment and would be akin to a wild spikes removal where individual pixels are reassigned nearby neighbors when they are completely surrounded by indexed pixels. 5 represents maximum treatment tested here. 1 would be the highest overall, where if one neighboring pixel has an index value, the non-indexed pixel would be assigned a value. Data is taken from Qi et al. (2015). This filter is available in Chanel5 software, and data processing of EBSD prior to grain reconstruction in MTEX was largely assisted by Dr. Jessica Warren from University of Delaware.
The testing of this filter is applied to several regions defined below, either inside the melt band or outside. Each treatment in each region has, in the top left, the total EBSD image and scale bar, on the right the region selected in the red box with reconstructed grains, and below a histogram of the log-grain size data with a best fit applied. These images correspond to table 2 in the main text.

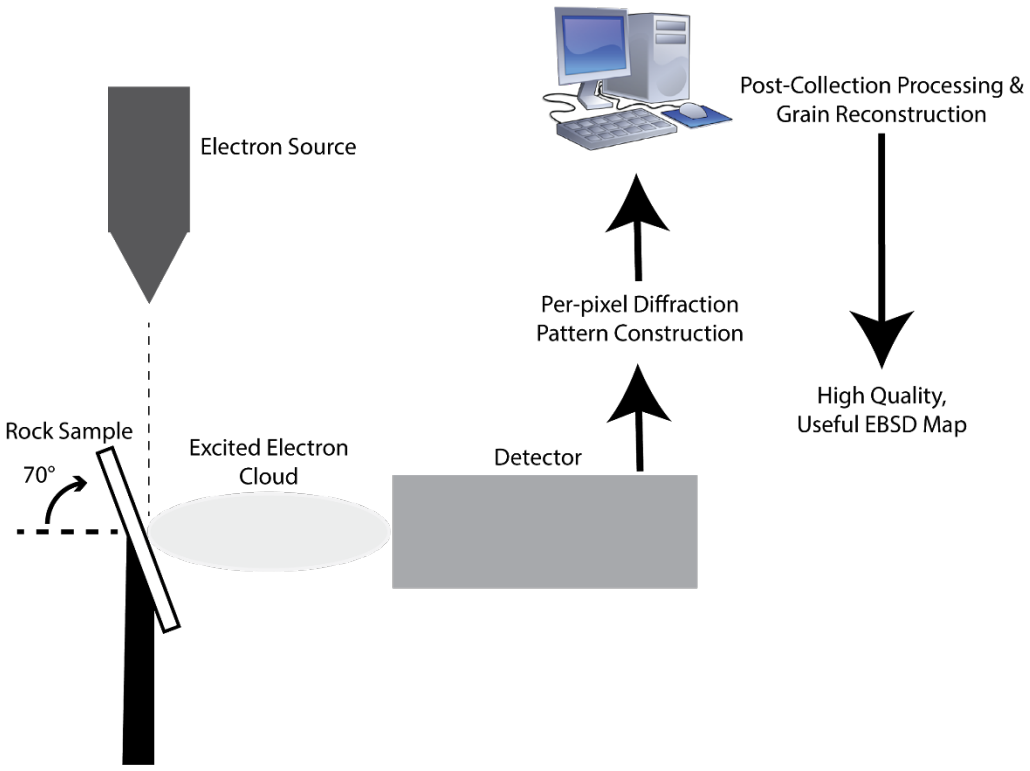

Figure A1: An overview of EBSD methodology. Polished rock sample is loaded and pelted with electrons, where the excited electron cloud is picked up by a detector, and

diffraction patterns are reconstructed by collection software. Pixel orientations of a mapped area can then be exported and processed.

Inside-Band Region One- 8 Neighbor Treatment

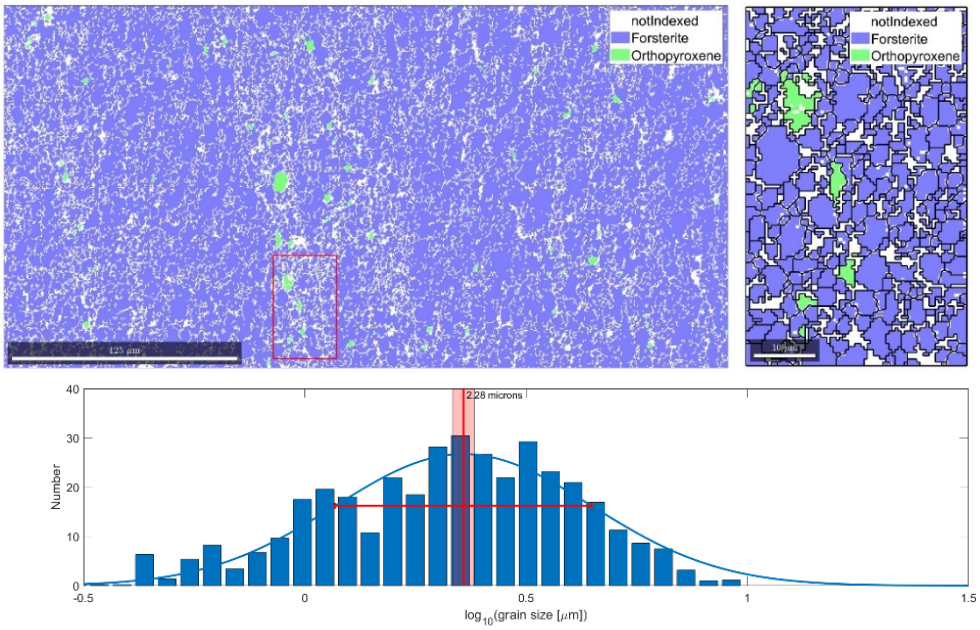

Figure A2: Top left: EBSD data. Top right: Grain reconstruction of the region boxed in red from the EBSD data. Bottom: Histogram of grain size. The mean grain size of 2.28 μm from the best fit of the histogram is reported in Table 2.

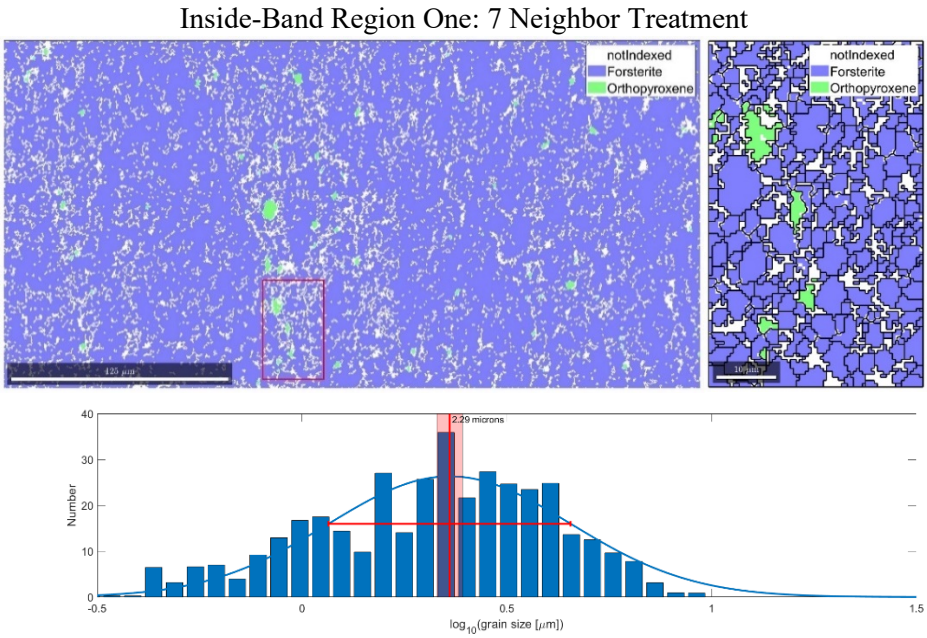

Figure A3: Top left: EBSD data. Top right: Grain reconstruction of the region boxed in red from the EBSD data. Bottom: Histogram of grain size. The mean grain size of 2.29 μm from the best fit of the histogram is reported in Table 2.

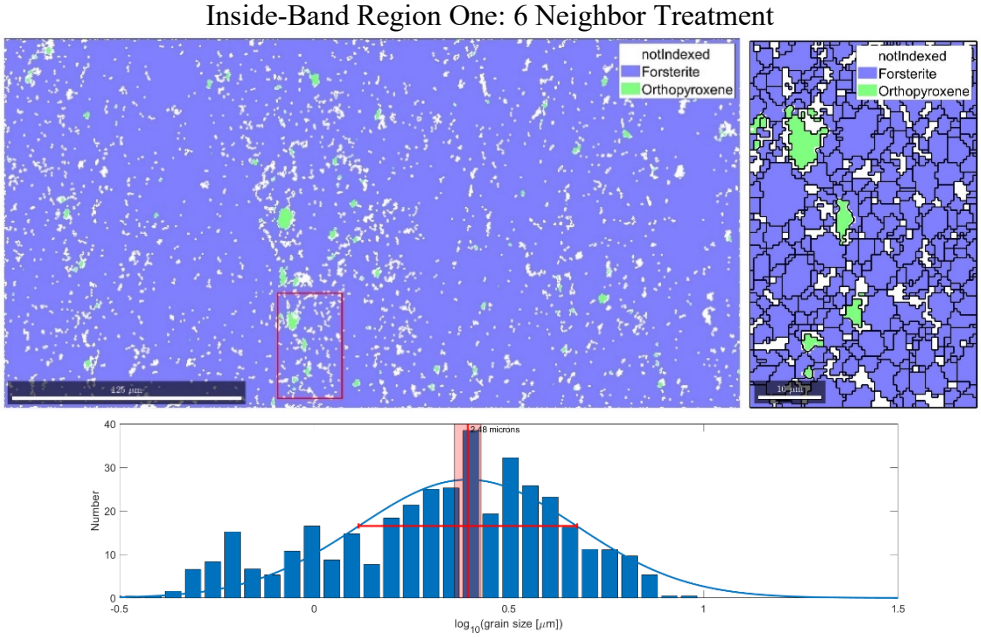

Figure A4: Top left: EBSD data. Top right: Grain reconstruction of the region boxed in red from the EBSD data. Bottom: Histogram of grain size. The mean grain size of 2.48 μm from the best fit of the histogram is reported in Table 2.

Inside-Band Region One: 5 Neighbor Treatment

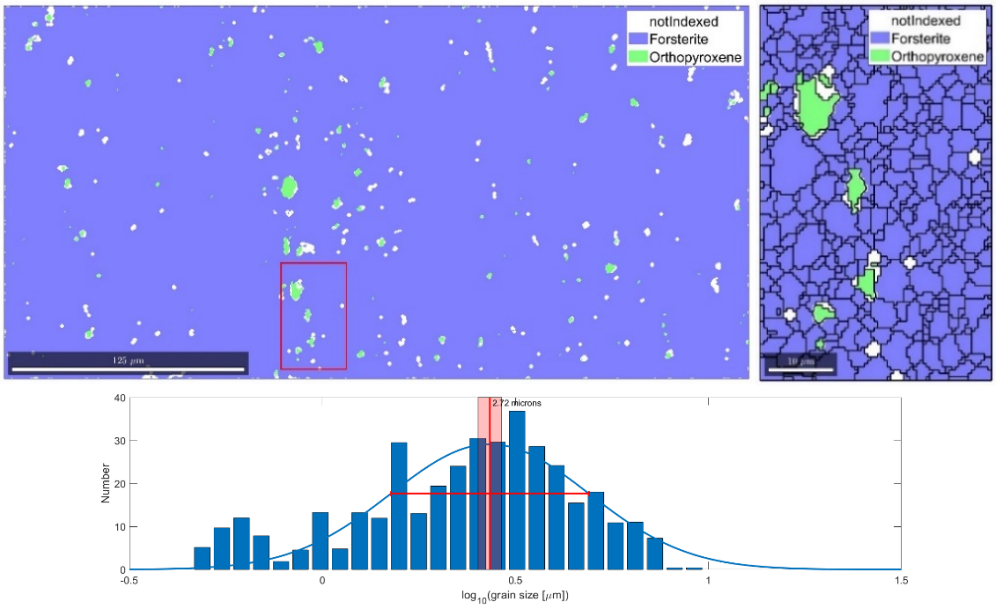

Figure A5: Top left: EBSD data. Top right: Grain reconstruction of the region boxed in red from the EBSD data. Bottom: Histogram of grain size. The mean grain size of 2.72 µm from the best fit of the histogram is reported in Table 2.

Inside-Band region two: 8 Neighbor Treatment

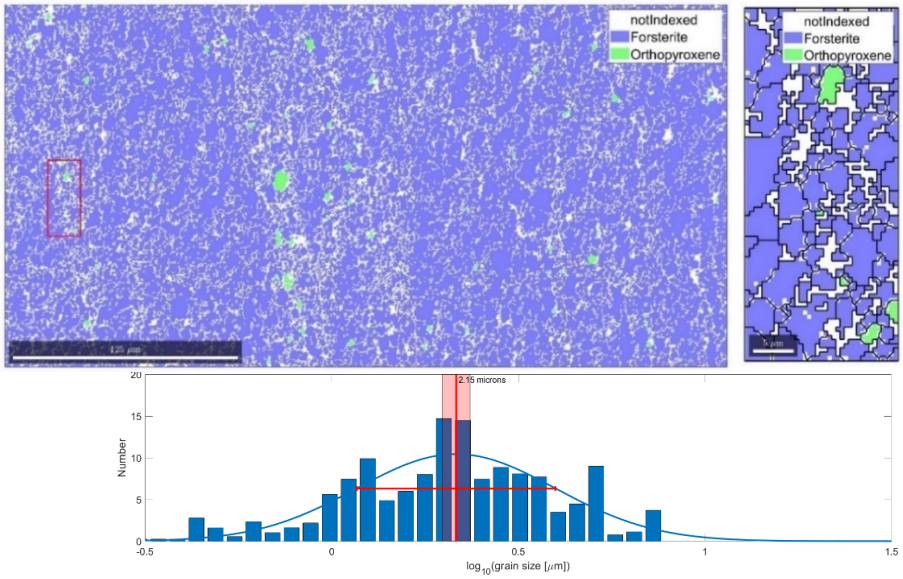

Figure A6: Top left: EBSD data. Top right: Grain reconstruction of the region boxed in red from the EBSD data. Bottom: Histogram of grain size. The mean grain size of 2.15 µm from the best fit of the histogram is reported in Table 2.

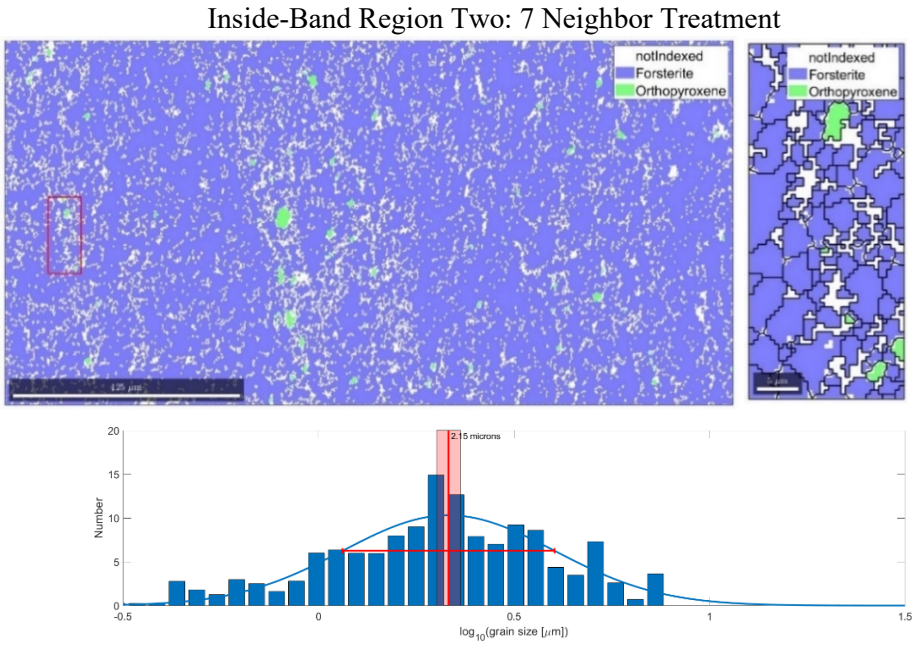

Figure A7: Top left: EBSD data. Top right: Grain reconstruction of the region boxed in red from the EBSD data. Bottom: Histogram of grain size. The mean grain size of 2.15 μm from the best fit of the histogram is reported in Table 2.

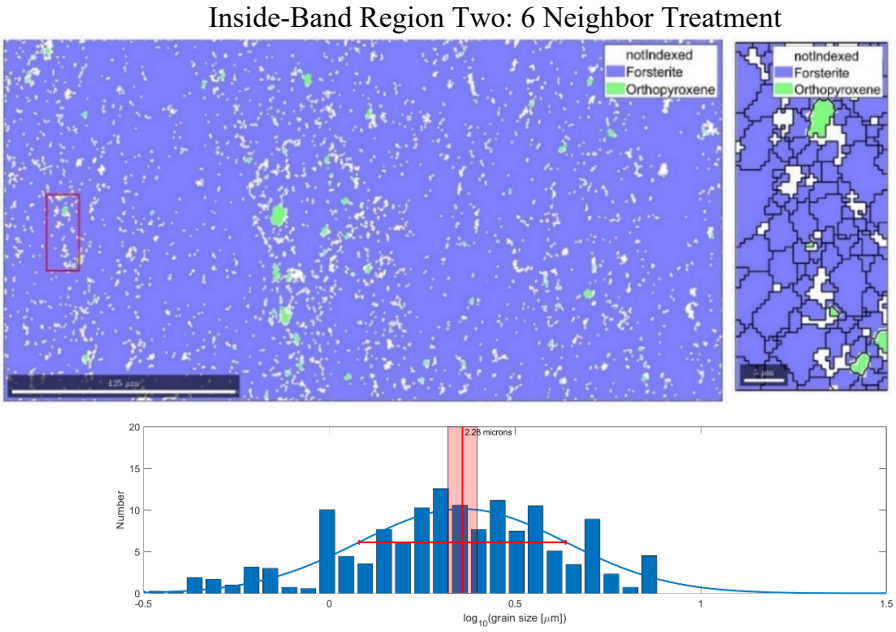

Figure A8: Top left: EBSD data. Top right: Grain reconstruction of the region boxed in red from the EBSD data. Bottom: Histogram of grain size. The mean grain size of 2.28 μm from the best fit of the histogram is reported in Table 2.

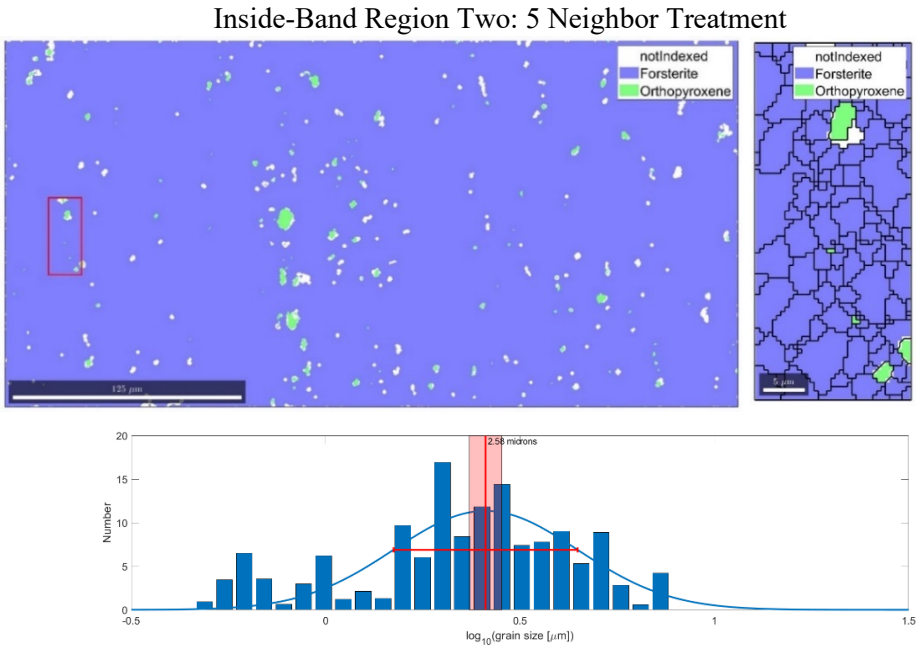

Figure A9: Top left: EBSD data. Top right: Grain reconstruction of the region boxed in red from the EBSD data. Bottom: Histogram of grain size. The mean grain size of 2.58 μm from the best fit of the histogram is reported in Table 2.

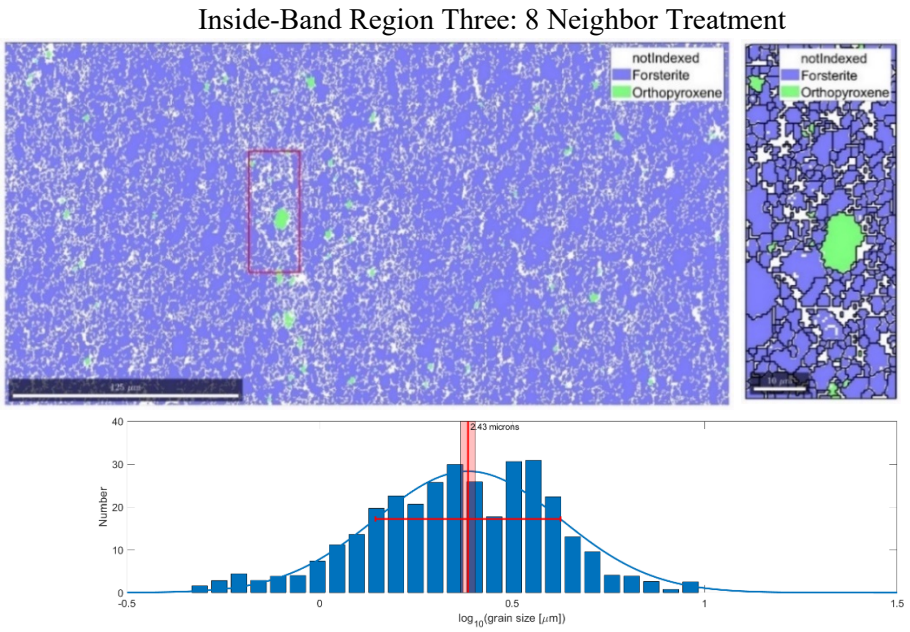

Figure A10: Top left: EBSD data. Top right: Grain reconstruction of the region boxed in red from the EBSD data. Bottom: Histogram of grain size. The mean grain size of 2.43 μm from the best fit of the histogram is reported in Table 2.

Inside-Band Region Three: 7 Neighbor Treatment

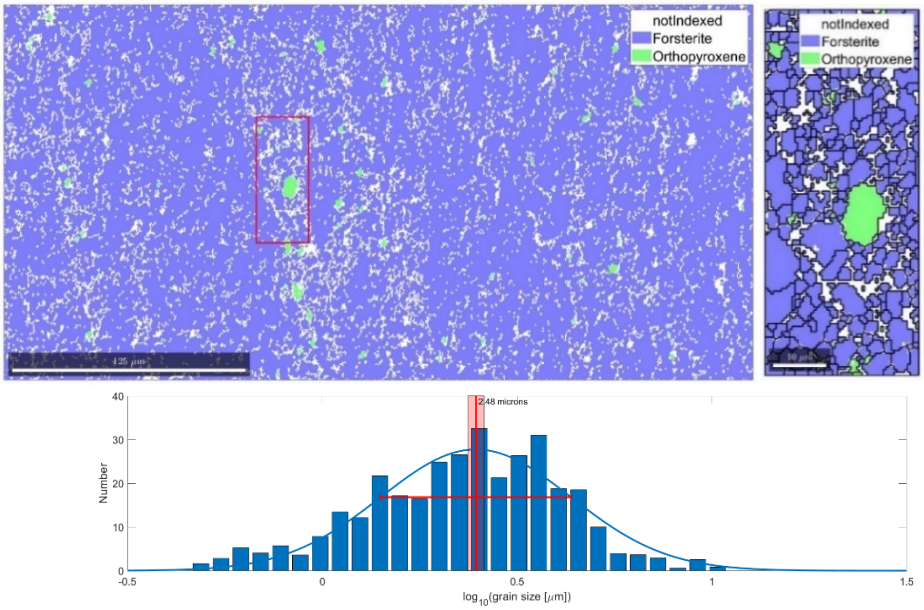

Figure A11: Top left: EBSD data. Top right: Grain reconstruction of the region boxed in red from the EBSD data. Bottom: Histogram of grain size. The mean grain size of 2.48 μm from the best fit of the histogram is reported in Table 2.

Inside-Band Region Three: 6 Neighbor Treatment:

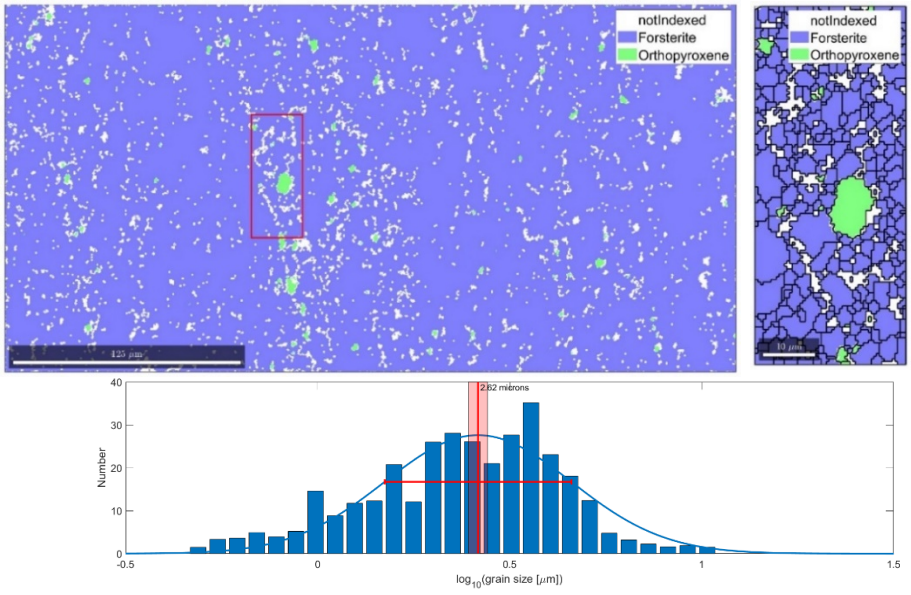

Figure A12: Top left: EBSD data. Top right: Grain reconstruction of the region boxed in red from the EBSD data. Bottom: Histogram of grain size. The mean grain size of 2.62 μm from the best fit of the histogram is reported in Table 2.

Inside-Band Region Three: 5 Neighbor Treatment

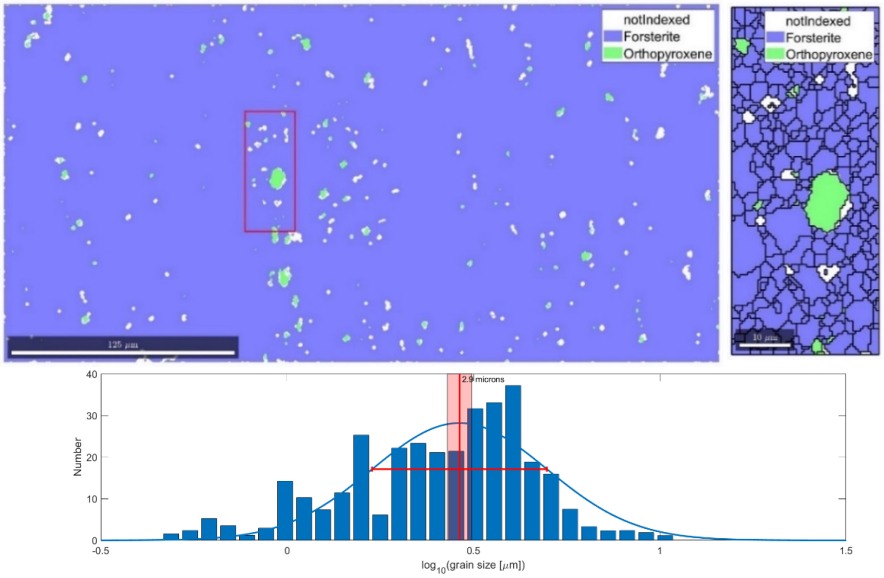

Figure A13: Top left: EBSD data. Top right: Grain reconstruction of the region boxed in red from the EBSD data. Bottom: Histogram of grain size. The mean grain size of 2.90 µm from the best fit of the histogram is reported in Table 2.

Outside-Band Region One: 8 Neighbor Treatment

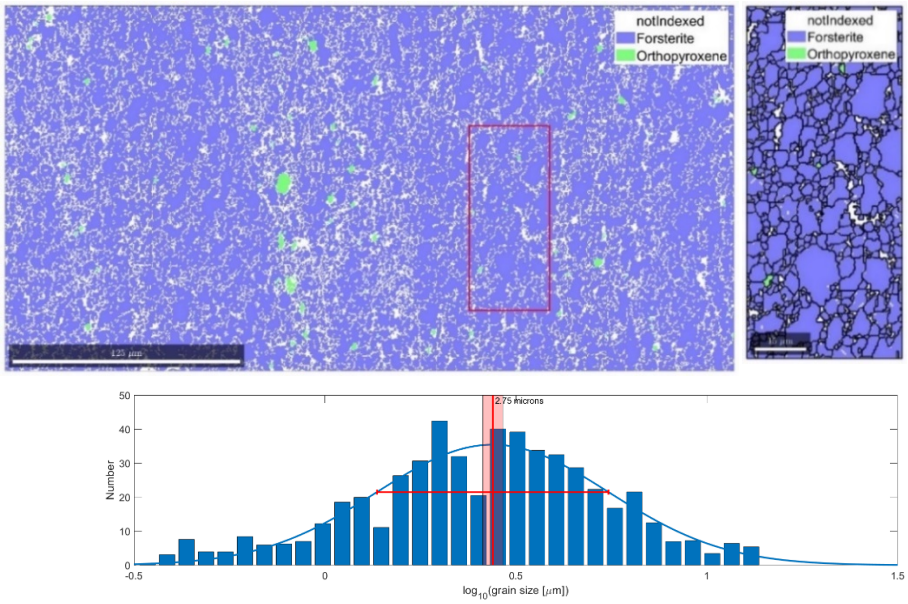

Figure A14: Top left: EBSD data. Top right: Grain reconstruction of the region boxed in red from the EBSD data. Bottom: Histogram of grain size. The mean grain size of 2.75 µm from the best fit of the histogram is reported in Table 2.

Outside-Band Region One: 7 Neighbor Treatment

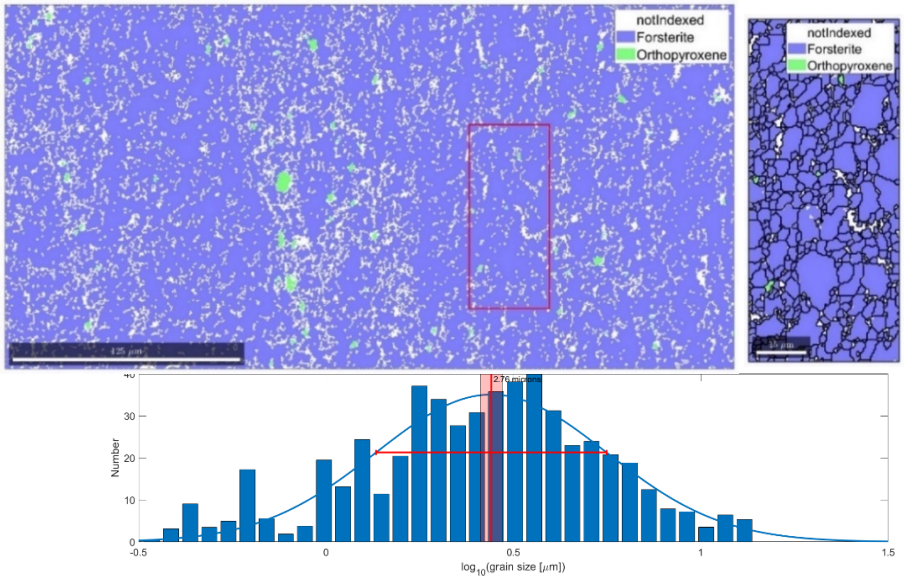

Figure A15: Top left: EBSD data. Top right: Grain reconstruction of the region boxed in red from the EBSD data. Bottom: Histogram of grain size. The mean grain size of 2.76 μm from the best fit of the histogram is reported in Table 2.

Outside-Band Region One: 6 Neighbor Treatment

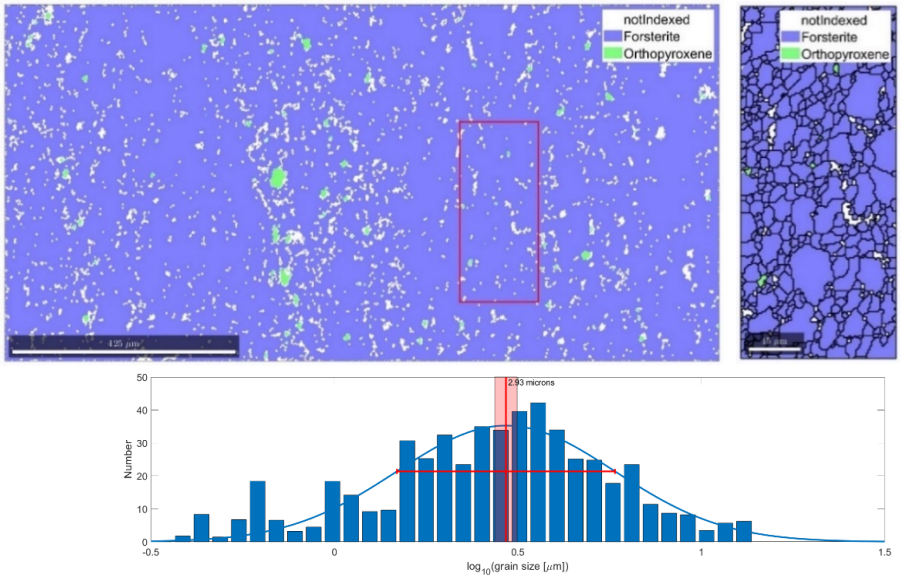

Figure A16: Top left: EBSD data. Top right: Grain reconstruction of the region boxed in red from the EBSD data. Bottom: Histogram of grain size. The mean grain size of 2.93 μm from the best fit of the histogram is reported in Table 2.

Outside-Band Region One: 5 Neighbor Treatment

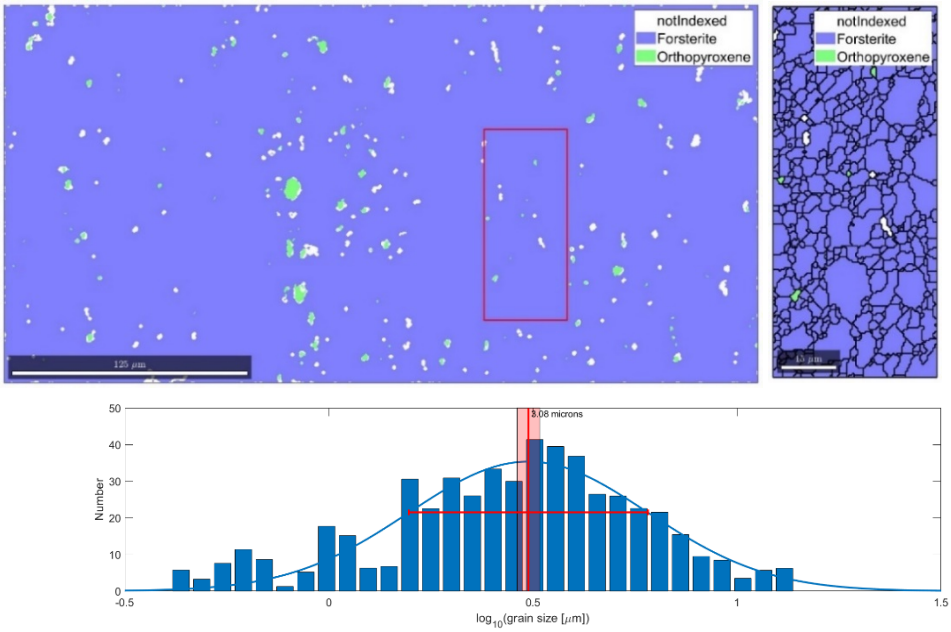

Figure A17: Top left: EBSD data. Top right: Grain reconstruction of the region boxed in red from the EBSD data. Bottom: Histogram of grain size. The mean grain size of 3.08 μm from the best fit of the histogram is reported in Table 2.

Bibliography

Ahern, J. L., & Turcotte, D. L. (1979). Magma migration beneath an ocean ridge. *Earth and Planetary Science Letters*, *45*(1), 115–122. https://doi.org/10.1016/0012-821X(79)90113-4

Bachmann, F., Hielscher, R., & Schaeben, H. (2010). Texture Analysis with MTEX – Free and Open Source Software Toolbox. *Solid State Phenomena*, *160*, 63–68. https://doi.org/10.4028/www.scientific.net/SSP.160.63

Bargen, N. von, & Waff, H. S. (1986). Permeabilities, interfacial areas and curvatures of partially molten systems: Results of numerical computations of equilibrium microstructures. *Journal of Geophysical Research: Solid Earth*, *91*(B9), 9261–9276. https://doi.org/10.1029/JB091iB09p09261

Bernsdorf, J., Durst, F., & Schäfer, M. (1999). Comparison of cellular automata and finite volume techniques for simulation of incompressible flows in complex geometries. *International Journal for Numerical Methods in Fluids*, *29*(3), 251–264. https://doi.org/10.1002/(SICI)1097-0363(19990215)29:3<251::AID-FLD783>3.0.CO;2-L

Boek, E. S., & Venturoli, M. (2010). Lattice-Boltzmann studies of fluid flow in porous media with realistic rock geometries. *Computers & Mathematics with Applications*, *59*(7), 2305–2314. https://doi.org/10.1016/j.camwa.2009.08.063

Braun, M. G., & Kelemen, P. B. (2002). Dunite distribution in the Oman Ophiolite: Implications for melt flux through porous dunite conduits: DUNITE

DISTRIBUTION IN THE OMAN OPHIOLITE. *Geochemistry, Geophysics, Geosystems*, *3*(11), 1–21. https://doi.org/10.1029/2001GC000289

Butler, S. L. (2009). The effects of buoyancy on shear-induced melt bands in a compacting porous medium. *Physics of the Earth and Planetary Interiors*, *173*(1), 51–59. https://doi.org/10.1016/j.pepi.2008.10.022

Cmíral, M., Gerald, J. D. F., Faul, U. H., & Green, D. H. (1998). A close look at dihedral angles and melt geometry in olivine-basalt aggregates: a TEM study. *Contributions to Mineralogy and Petrology*, *130*(3), 336–345. https://doi.org/10.1007/s004100050369

Daines, M. J., & Kohlstedt, D. L. (1997). Influence of deformation on melt topology in peridotites. *Journal of Geophysical Research: Solid Earth*, *102*(B5), 10257–10271. https://doi.org/10.1029/97JB00393

Dunn, R. A., Arai, R., Eason, D. E., Canales, J. P., & Sohn, R. A. (2017). Three-Dimensional Seismic Structure of the Mid-Atlantic Ridge: An Investigation of Tectonic, Magmatic, and Hydrothermal Processes in the Rainbow Area: Mid-Atlantic Ridge Seismic Structure. *Journal of Geophysical Research: Solid Earth*, *122*(12), 9580–9602. https://doi.org/10.1002/2017JB015051

Forsyth, D. W., & Scheirer, D. S. (1998). Imaging the deep seismic structure beneath a mid-ocean ridge: the MELT experiment. *Science*, *280*(5367), 1215–1220.

Frey, F. A., Bryan, W. B., & Thompson, G. (1974). Atlantic ocean floor: Geochemistry and petrology of basalts from legs 2 and 3 of the Deep-Sea Drilling Project. *Journal of Geophysical Research (1896-1977)*, *79*(35), 5507–5527. https://doi.org/10.1029/JB079i035p05507

Hansen, L. N., Warren, J. M., Zimmerman, M. E., & Kohlstedt, D. L. (2016). Viscous anisotropy of textured olivine aggregates, Part 1: Measurement of the magnitude and evolution of anisotropy. *Earth and Planetary Science Letters*, *445*, 92–103. https://doi.org/10.1016/j.epsl.2016.04.008

Hebert, L. B., & Montési, L. G. J. (2010). Generation of permeability barriers during melt extraction at mid-ocean ridges. *Geochemistry, Geophysics, Geosystems*, *11*(12). https://doi.org/10.1029/2010GC003270

Holtzman, B. K. (2003). Melt Segregation and Strain Partitioning: Implications for Seismic Anisotropy and Mantle Flow. *Science*, *301*(5637), 1227–1230. https://doi.org/10.1126/science.1087132

Holtzman, B. K., & Kohlstedt, D. L. (2007). Stress-driven Melt Segregation and Strain Partitioning in Partially Molten Rocks: Effects of Stress and Strain. *Journal of Petrology*, *48*(12), 2379–2406. https://doi.org/10.1093/petrology/egm065

Holtzman, B. K., Groebner, N. J., Zimmerman, M. E., Ginsberg, S. B., & Kohlstedt, D. L. (2003). Stress-driven melt segregation in partially molten rocks. *Geochemistry, Geophysics, Geosystems*, *4*(5). https://doi.org/10.1029/2001GC000258

Katz, R. F., Spiegelman, M., & Holtzman, B. (2006). The dynamics of melt and shear localization in partially molten aggregates. *Nature*, *442*(7103), 676–679. https://doi.org/10.1038/nature05039

Kelemen, P. B., Shimizu, N., & Salters, V. J. M. (1995). Extraction of mid-ocean-ridge basalt from the upwelling mantle by focused flow of melt in dunite channels. *Nature*, *375*(6534), 747–753. https://doi.org/10.1038/375747a0

Key, K., & Constable, S. (2002). Broadband marine MT exploration of the East Pacific Rise at 9°50′N. *Geophysical Research Letters*, *29*(22), 11-1-11–4. https://doi.org/10.1029/2002GL016035

King, D. S. H., Zimmerman, M. E., & Kohlstedt, D. L. (2010). Stress-driven Melt Segregation in Partially Molten Olivine-rich Rocks Deformed in Torsion. *Journal of Petrology*, *51*(1–2), 21–42. https://doi.org/10.1093/petrology/egp062

Kohlstedt, D. L., & Holtzman, B. K. (2009). Shearing Melt Out of the Earth: An Experimentalist's Perspective on the Influence of Deformation on Melt Extraction. *Annual Review of Earth and Planetary Sciences*, *37*(1), 561–593. https://doi.org/10.1146/annurev.earth.031208.100104

Lundstrom, C. (2000). Models of U-series disequilibria generation in MORB: the effects of two scales of melt porosity. *Physics of the Earth and Planetary Interiors*, *121*(3), 189–204. https://doi.org/10.1016/S0031-9201(00)00168-0

Lundstrom, C. C., Williams, Q., & Gill, J. B. (1998). Investigating solid mantle upwelling rates beneath mid-ocean ridges using U-series disequilibria, 1: a global approach. *Earth and Planetary Science Letters*, *157*(3), 151–165. https://doi.org/10.1016/S0012-821X(98)00038-7

Lundstrom, C. C., Sampson, D. E., Perfit, M. R., Gill, J., & Williams, Q. (1999). Insights into mid-ocean ridge basalt petrogenesis: U-series disequilibria from the Siqueiros Transform, Lamont Seamounts, and East Pacific Rise. *Journal of Geophysical Research: Solid Earth*, *104*(B6), 13035–13048. https://doi.org/10.1029/1999JB900081

Mantle Melting and Basalt Extraction by Equilibrium Porous Flow | Science. (n.d.). Retrieved August 11, 2020, from https://science-sciencemag-org.proxy-um.researchport.umd.edu/content/270/5244/1958.abstract

McKENZIE, D. (1984). The Generation and Compaction of Partially Molten Rock. *Journal of Petrology*, *25*(3), 713–765. https://doi.org/10.1093/petrology/25.3.713

Melting in the oceanic upper mantle: An ion microprobe study of diopsides in abyssal peridotites - Johnson - 1990 - Journal of Geophysical Research: Solid Earth - Wiley Online Library. (n.d.). Retrieved August 11, 2020, from https://agupubs-onlinelibrary-wiley-com.proxy-um.researchport.umd.edu/doi/abs/10.1029/JB095iB03p02661

Miller, K. J., Zhu, W., Montési, L. G. J., & Gaetani, G. A. (2014). Experimental quantification of permeability of partially molten mantle rock. *Earth and Planetary Science Letters*, *388*, 273–282. https://doi.org/10.1016/j.epsl.2013.12.003

Miller, K. J., Zhu, W., Montési, L. G. J., Gaetani, G. A., Roux, V. L., & Xiao, X. (2016). Experimental evidence for melt partitioning between olivine and orthopyroxene in partially molten harzburgite. *Journal of Geophysical Research: Solid Earth*, *121*(8), 5776–5793. https://doi.org/10.1002/2016JB013122

Qi, C. (2018). Stress-driven melt redistribution in partially molten rocks deformed in torsion: from pressure shadows to base-state segregation. *University of Minnesota PhD Thesis*.

Qi, C., Kohlstedt, D. L., Katz, R. F., & Takei, Y. (2015). Experimental test of the viscous anisotropy hypothesis for partially molten rocks. *Proceedings of the National*

Academy of Sciences, *112*(41), 12616–12620. https://doi.org/10.1073/pnas.1513790112

Qi, C., Hansen, L. N., Wallis, D., Holtzman, B. K., & Kohlstedt, D. L. (2018). Crystallographic Preferred Orientation of Olivine in Sheared Partially Molten Rocks: The Source of the "a-c Switch." *Geochemistry, Geophysics, Geosystems*, *19*(2), 316–336. https://doi.org/10.1002/2017GC007309

Salters, V. J. M., & Longhi, J. (1999). Trace element partitioning during the initial stages of melting beneath mid-ocean ridges. *Earth and Planetary Science Letters*, *166*(1), 15–30. https://doi.org/10.1016/S0012-821X(98)00271-4

Sim, S. (2018). *The depth of mid-ocean ridges through Earth's evolution and a two-phase study of melt focusing at mid-ocean ridges*. UC San Diego. Retrieved from https://escholarship.org/uc/item/38n3762m

Spiegelman, M. (2003). Linear analysis of melt band formation by simple shear. *Geochemistry, Geophysics, Geosystems*, *4*(9). https://doi.org/10.1029/2002GC000499

Spiegelman, M., Kelemen, P. B., & Aharonov, E. (2001). Causes and consequences of flow organization during melt transport: The reaction infiltration instability in compactible media. *Journal of Geophysical Research: Solid Earth*, *106*(B2), 2061–2077. https://doi.org/10.1029/2000JB900240

Takei, Y. (2010). Stress-induced anisotropy of partially molten rock analogue deformed under quasi-static loading test. *Journal of Geophysical Research: Solid Earth*, *115*(B3). https://doi.org/10.1029/2009JB006568

Weickert, J. (1999). Coherence-Enhancing Diffusion Filtering. *International Journal of Computer Vision*, *31*(2), 111–127. https://doi.org/10.1023/A:1008009714131

Zhu, W., Gaetani, G. A., Fusseis, F., Montesi, L. G. J., & De Carlo, F. (2011). Microtomography of Partially Molten Rocks: Three-Dimensional Melt Distribution in Mantle Peridotite. *Science*, *332*(6025), 88–91. https://doi.org/10.1126/science.1202221

Zhu, Wenlu, & Hirth, G. (2003). A network model for permeability in partially molten rocks. *Earth and Planetary Science Letters*, *212*(3), 407–416. https://doi.org/10.1016/S0012-821X(03)00264-4

Zimmerman, M. E., Zhang, S., Kohlstedt, D. L., & Karato, S. (1999). Melt distribution in mantle rocks deformed in shear. *Geophysical Research Letters*, *26*(10), 1505–1508. https://doi.org/10.1029/1999GL900259